Article

Immunity

Sublethal necroptosis signaling promotes inflammation and liver cancer

Graphical abstract

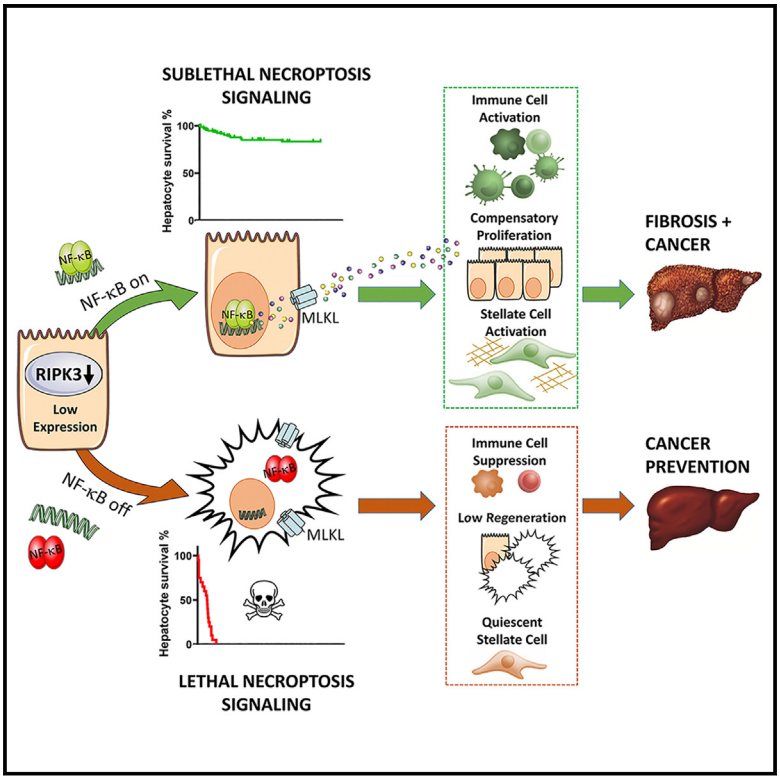

Highlights

- Low RIPK3 expression in hepatocytes enables sublethal necrosome activation *in vivo*
- Sublethal necroptosis signaling triggers cytokine release, fueling hepatocarcinogenesis
- NF-κB inhibition promotes lethal necroptosis, preventing cytokine release and HCC
- Converting sublethal to lethal necroptosis represents an anticancer strategy in the liver

Authors

Mihael Vucur, Ahmed Ghallab, Anne T. Schneider, ..., Jan G. Hengstler, Mathias Heikenwalder, Tom Luedde

Correspondence

vucur@hhu.de (M.V.), luedde@hhu.de (T.L.)

In brief

The role of necroptosis in cancer development is not well understood. Vucur et al. show that in hepatocytes with low RIPK3 expression, parallel NF-κB activation triggers sublethal necrosome activation, driving inflammation and hepatocarcinogenesis. Switching to lethal necroptosis through NF-κB inhibition limits immune responses and prevents liver cancer.

Vucur et al., 2023, Immunity *56*, 1578–1595
July 11, 2023
https://doi.org/10.1016/j.immuni.2023.05.017

CellPress

CellPress
OPEN ACCESS

Immunity

Article

Sublethal necroptosis signaling promotes inflammation and liver cancer

Mihael Vucur,[1,*] Ahmed Ghallab,[2,3] Anne T. Schneider,[1] Arlind Adili,[4] Mingbo Cheng,[5] Mirco Castoldi,[1] Michael T. Singer,[1] Veronika Büttner,[1] Leonie S. Keysberg,[1] Lena Küsgens,[1] Marlene Kohlhepp,[6] Boris Görg,[1] Suchira Gallage,[4,7] Jose Efren Barragan Avila,[4] Kristian Unger,[8] Claus Kordes,[1] Anne-Laure Leblond,[9] Wiebke Albrecht,[2] Sven H. Loosen,[1] Carolin Lohr,[1] Markus S. Jördens,[1] Anne Babler,[10] Sikander Hayat,[10] David Schumacher,[10] Maria T. Koenen,[11] Olivier Govaere,[12] Mark V. Boekschoten,[13] Simone Jörs,[14] Carlos Villacorta-Martin,[15] Vincenzo Mazzaferro,[16] Josep M. Llovet,[15,17,18] Ralf Weiskirchen,[19] Jakob N. Kather,[20] Patrick Starlinger,[21] Michael Trauner,[22] Mark Luedde,[23]

(Author list continued on next page)

[1]Department of Gastroenterology, Hepatology and Infectious Diseases, University Hospital Dusseldorf, Medical Faculty at Heinrich Heine University Dusseldorf, Dusseldorf, Germany
[2]Leibniz Research Centre for Working Environment and Human Factors (IfADo), Technical University Dortmund, Dortmund, Germany
[3]Department of Forensic Medicine and Toxicology, Faculty of Veterinary Medicine, South Valley University, Qena, Egypt
[4]Department of Chronic Inflammation and Cancer, German Cancer Research Institute (DKFZ), Heidelberg, Germany
[5]Institute for Computational Genomics, RWTH Aachen University, Aachen, Germany
[6]Department of Hepatology and Gastroenterology, Charité—Universitätsmedizin Berlin, Campus Virchow Klinikum and Campus Charité Mitte, Berlin, Germany
[7]The M3 Research Institute, Eberhard Karls University, Tübingen, Germany
[8]Research Unit of Radiation Cytogenetics, Helmholtz Zentrum München, German Research Center for Environmental Health, Neuherberg, Germany
[9]Department for pathology and molecular pathology, Zürich University Hospital, Zürich, Switzerland
[10]Institute of Experimental Medicine and Systems Biology and Department of Nephrology, RWTH Aachen University, Medical Faculty, Aachen, Germany
[11]Department of Medicine, Rhein-Maas-Klinikum, Würselen, Germany
[12]Department of Imaging and Pathology, KU Leuven and University Hospitals Leuven, Leuven, Belgium
[13]Nutrition, Metabolism and Genomics Group, Division of Human Nutrition and Health, Wageningen University, Wageningen, the Netherlands
[14]Second Department of Internal Medicine, Klinikum Rechts der Isar, Technische Universität München, Germany
[15]Division of Liver Diseases, Liver Cancer Program, Department of Medicine, Tisch Cancer Institute, Icahn School of Medicine at Mount Sinai, New York, NY, USA
[16]Gastrointestinal Surgery and Liver Transplantation Unit, National Cancer Institute, University of Milan, Milan, Italy

(Affiliations continued on next page)

SUMMARY

It is currently not well known how necroptosis and necroptosis responses manifest *in vivo*. Here, we uncovered a molecular switch facilitating reprogramming between two alternative modes of necroptosis signaling in hepatocytes, fundamentally affecting immune responses and hepatocarcinogenesis. Concomitant necrosome and NF-κB activation in hepatocytes, which physiologically express low concentrations of receptor-interacting kinase 3 (RIPK3), did not lead to immediate cell death but forced them into a prolonged "sublethal" state with leaky membranes, functioning as secretory cells that released specific chemokines including CCL20 and MCP-1. This triggered hepatic cell proliferation as well as activation of procarcinogenic monocyte-derived macrophage cell clusters, contributing to hepatocarcinogenesis. In contrast, necrosome activation in hepatocytes with inactive NF-κB-signaling caused an accelerated execution of necroptosis, limiting alarmin release, and thereby preventing inflammation and hepatocarcinogenesis. Consistently, intratumoral NF-κB-necroptosis signatures were associated with poor prognosis in human hepatocarcinogenesis. Therefore, pharmacological reprogramming between these distinct forms of necroptosis may represent a promising strategy against hepatocellular carcinoma.

INTRODUCTION

Cancer development and response to therapy are strongly influenced by innate and adaptive immunity.[1] Hepatocellular carcinoma (HCC), the common end stage of chronic liver diseases, arises almost exclusively in the context of chronic hepatic inflammation.[2] Hepatocellular death occurs in almost all types of human liver disease and represents the most critical molecular

Lara R. Heij,[24] Ulf P. Neumann,[24] Verena Keitel,[1,25] Johannes G. Bode,[1] Rebekka K. Schneider,[26] Frank Tacke,[6] Bodo Levkau,[27] Twan Lammers,[28] Georg Fluegen,[29] Theodore Alexandrov,[30] Amy L. Collins,[31] Glyn Nelson,[31] Fiona Oakley,[31] Derek A. Mann,[31] Christoph Roderburg,[1] Thomas Longerich,[32] Achim Weber,[9] Augusto Villanueva,[15,33] Andre L. Samson,[34,35] James M. Murphy,[34,35] Rafael Kramann,[10] Fabian Geisler,[14] Ivan G. Costa,[5] Jan G. Hengstler,[2,36] Mathias Heikenwalder,[4,7,36] and Tom Luedde[1,37,38,*]

[17]Liver Cancer Translational Research Laboratory, Barcelona-Clínic Liver Cancer Group, Institut d'Investigacions Biomèdiques August Pi i Sunyer (IDIBAPS), Liver Unit, CIBEREHD, Hospital Clínic, Barcelona, Catalonia, Spain
[18]Institució Catalana de Recerca i Estudis Avançats (ICREA), Barcelona, Spain
[19]Institute of Molecular Pathobiochemistry, Experimental Gene Therapy and Clinical Chemistry (IFMPEGKC), University Hospital RWTH Aachen, Aachen, Germany
[20]Else Kroener Fresenius Center for Digital Health, Medical Faculty Carl Gustav Carus, Technical University Dresden, Dresden, Germany
[21]Department of Surgery, Division of Hepatobiliary and Pancreatic Surgery, Mayo Clinic, Rochester, MN, USA
[22]Division of Gastroenterology and Hepatology, Department of Medicine III, Medical University of Vienna, Vienna, Austria
[23]Department of Cardiology and Angiology, University Hospital Schleswig-Holstein, Kiel, Germany
[24]Visceral and Transplant Surgery, University Hospital RWTH Aachen, Aachen, Germany
[25]Department of Gastroenterology, Hepatology and Infectious Diseases, University Hospital Magdeburg, Medical Faculty of Otto Von Guericke University Magdeburg, Magdeburg, Germany
[26]Department of Cell Biology, Institute for Biomedical Engineering, Faculty of Medicine, RWTH Aachen University, Aachen, Germany
[27]Institute of Molecular Medicine III, University Hospital Dusseldorf, Heinrich Heine University, Dusseldorf, Germany
[28]Department of Nanomedicine and Theranostics, Institute for Experimental Molecular Imaging, Faculty of Medicine, RWTH Aachen University, Aachen, Germany
[29]Department of Surgery (A), University Hospital Dusseldorf, Medical Faculty at Heinrich Heine University, Dusseldorf, Germany
[30]Structural and Computational Biology Unit, European Molecular Biology Laboratory, Heidelberg, Germany
[31]Newcastle Fibrosis Research Group, Biosciences Institute, Newcastle University, Newcastle upon Tyne, UK
[32]Institute of Pathology, University Hospital Heidelberg, Heidelberg, Germany
[33]Division of Hematology and Medical Oncology, Department of Medicine, Icahn School of Medicine at Mount Sinai, New York, NY, USA
[34]The Walter and Eliza Hall Institute, Parkville, VIC, Australia
[35]Department of Medical Biology, University of Melbourne, Parkville, VIC, Australia
[36]These authors contributed equally
[37]Twitter: @tom_luedde
[38]Lead contact
*Correspondence: vucur@hhu.de (M.V.), luedde@hhu.de (T.L.)
https://doi.org/10.1016/j.immuni.2023.05.017

event related to inflammatory responses.[3] While many different forms of regulated cell death have been described so far, necroptosis in particular has been attributed a major role in driving metabolic liver diseases such as alcoholic and nonalcoholic steatohepatitis (ASH and NASH, respectively),[4,5] which are among the main causes for HCC development.[6] Necroptosis relies on the activation of the necrosome—a molecular complex consisting of the kinases receptor-interacting kinase 1 (RIPK1) and RIPK3 and the pseudokinase MLKL.[7,8]

In general, necroptosis is thought to be a highly reactive form of cell death triggering strong inflammation by the release of immunostimulatory intracellular components called damage-associated molecular patterns (DAMPs), which are exposed to immune cells after cell-membrane rupture.[9] However, it is currently unclear whether an MLKL-activated cell always executes cell death or if sublethal forms of necroptosis exist.[10–12] This may be important considering that necroptosis execution, DAMP-release, immune-cell activation, and thus the long-term biological consequences of necroptosis activation could vary substantially in a given disease context.[11] To date, there are very few examples of clinical trials targeting necroptosis in human disease,[13] which is mainly due to the fact that it is difficult to unequivocally detect necroptotic cell death in human disease.[14,15] Moreover, there is a potential risk that necroptosis targeting may inadvertently activate alternative cell-death forms.[16,17]

Here, we show that a molecular switch exists in hepatocytes that determines the mode of execution as well as the biological responses following activation of the necroptosis pathway *in vivo*, thereby promoting or inhibiting immune-cell activation and subsequent hepatocarcinogenesis. Reprogramming of necroptosis responses, rather than inhibiting necroptosis itself, could therefore represent a strategy to prevent cancer development in patients with chronic liver diseases.

RESULTS

Chronic activation of the necroptosis pathway in liver parenchymal cells correlates with remodeling of the hepatobiliary architecture

We ablated *Traf2*—an adapter protein for the E3-ubiquitin-ligases cIAP1 and cIAP2[18,19] inhibiting apoptosis and necroptosis[20]—in liver parenchymal cells LPC$^{\Delta Traf2}$ (LPC) mice (Figure S1A). As expected,[21] this led to hepatitis, reflected by elevated serum concentrations of aspartate aminotransferase (AST), alanine aminotransferase (ALT), and glutamate dehydrogenase (GLDH) (Figure S1B). Histological analysis revealed no gross abnormalities, despite a pronounced ductular reaction in some portal tracts in LPC$^{\Delta Traf2}$ livers compared with wild-type (WT) controls (Figure S1C). Moreover, LPC$^{\Delta Traf2}$ livers showed spontaneous hepatocyte apoptosis demonstrated by immunohistochemistry (IHC) for cleaved caspase-3 (Figures S1D and S1E). We also treated LPC$^{\Delta Traf2}$ and WT mice with bacterial lipopolysaccharide (LPS), which resulted in pronounced apoptosis and liver injury in LPC$^{\Delta Traf2}$ but not in WT livers (Figures S1F–S1I). We also isolated

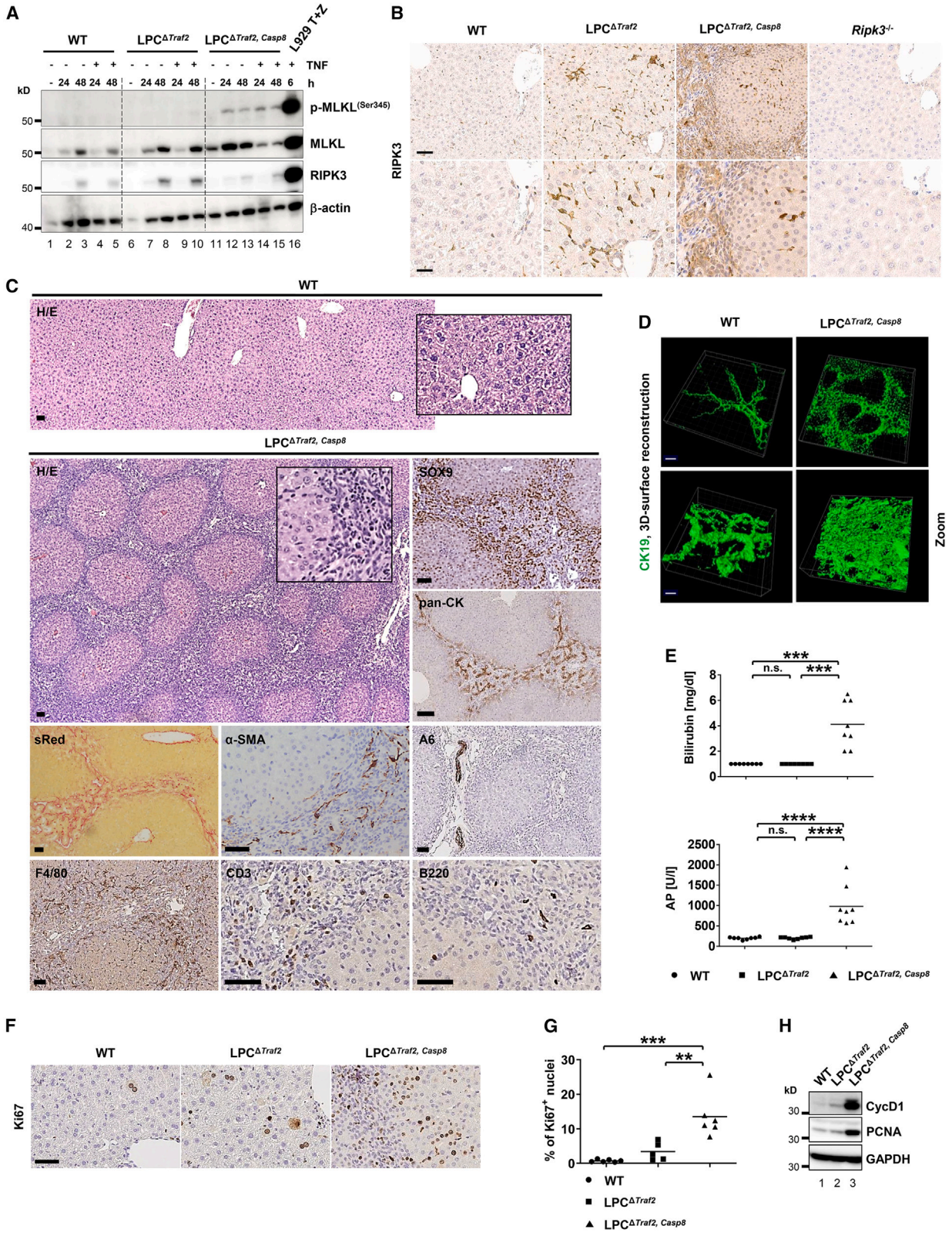

Figure 1. Chronic activation of necroptosis correlates with remodeling of the hepatobiliary architecture

(A) Immunoblot analysis of extracts from primary hepatocytes treated with TNF (50 ng/mL). L929 extracts stimulated with TNF (T) and zVAD (Z) were used as controls.

(legend continued on next page)

and stimulated primary hepatocytes from LPC$^{\Delta Traf2}$ mice with recombinant TNF, which led to strong activation of apoptosis, as well as slight phosphorylation of MLKL as a surrogate for necroptosis activation in TRAF2-deficient hepatocytes (Figure S1J).

To functionally dissect the specific role of necroptosis from apoptosis in the context of *Traf2*-deletion, we ablated *Casp8* in LPC$^{\Delta Traf2}$ mice to block apoptosis activation (LPC$^{\Delta Traf2,\ Casp8}$ mice) (Figure S2A). As expected, caspase-3 cleavage was only detected in hepatocytes of LPC$^{\Delta Traf2}$ mice, but not in LPC$^{\Delta Traf2,\ Casp8}$ mice (Figures S1D, S1E, and S2B). In line, markers of hepatocyte injury were markedly reduced in LPC$^{\Delta Traf2,\ Casp8}$ mice compared with LPC$^{\Delta Traf2}$ mice, suggesting that liver injury in LPC$^{\Delta Traf2}$ mice was partially caused by apoptosis (Figure S2C). However, LPC$^{\Delta Traf2,\ Casp8}$ mice still showed increased concentrations of ALT and AST indicating that liver injury was still present (Figure S2C).

To assess activation of necroptosis in LPC$^{\Delta Traf2,\ Casp8}$ mice, we performed immunoblot analyses on lysates from primary hepatocytes, which showed low RIPK3 expression (Figure 1A). An IHC analysis and quantification of RIPK3 expression in murine livers confirmed previous data[22] that RIPK3 was only weakly expressed in hepatocytes of WT livers compared with immune cells and was slightly increased in hepatocytes of LPC$^{\Delta Traf2}$ and LPC$^{\Delta Traf2,\ Casp8}$ mice, but still to a lesser extent than in immune cells and biliary cells (Figures 1B and S2D), respectively. Low RIPK3 expression in hepatocytes *in vivo* was confirmed by *in situ* hybridization (ISH) analysis (Figure S2E).

In line with low RIPK3 expression in primary hepatocytes, we detected low phosphorylation of MLKL in both the absence and presence of exogenous TNF (Figure 1A). Of note, LPC$^{\Delta Traf2,\ Casp8}$ hepatocytes showed increased *Tnf* mRNA expression, which may have contributed to MLKL phosphorylation over time in untreated hepatocytes (Figure S2F). To further investigate the role of TNF in liver injury in LPC$^{\Delta Traf2,\ Casp8}$ mice, we treated LPC$^{\Delta Traf2,\ Casp8}$ mice with the TNF inhibitor etanercept for 2 weeks. This experiment did not result in a significant improvement of liver injury (Figure S2G).

Histologically, 6-week-old LPC$^{\Delta Traf2,\ Casp8}$ mice displayed a severe spontaneous liver phenotype with advanced fibrosis and porto-portal bridging (Figure 1C). Analyses in younger mice showed a normal histology at postnatal day 1, arguing against a defect in embryonic development in LPC$^{\Delta Traf2,\ Casp8}$ mice (Figure S2H). Notably, porto-portal bridging was already detected in 21-day-old mice (Figure S2H). Immunohistochemical characterization of 6-week-old mice revealed that the Sirius red positive fibrous septa contained α-SMA-positive activated hepatic stellate cells, and a prominent pan-cytokeratin (CK)- and SOX9-positive, A6-negative ductular reaction (Figure 1C). Accordingly, biliary differentiation was confirmed by electron microscopy (Figure S2I). Three-dimensional surface-reconstruction of CK19 stainings revealed the strong extent of altered biliary architecture (Figure 1D). Consistently, serum concentrations of bilirubin and alkaline phosphatase (AP) were elevated in LPC$^{\Delta Traf2,\ Casp8}$ mice (Figure 1E). IHC stainings revealed that the mixed interportal infiltrate contained multiple immune cells (Figure 1C). Immune-cell infiltration in LPC$^{\Delta Traf2,\ Casp8}$ livers was associated with increased expression of TRAF2 and caspase-8 in an immunoblot analysis performed on whole-liver protein extracts (Figure S2J). However, IHC analysis of liver slides from 6-to-8-week old mice showed that caspase-8 was only expressed in nonparenchymal cells and absent in hepatocytes from LPC$^{\Delta Traf2,\ Casp8}$ mice (Figures S2K and S2L). In line, qRT-PCR analyses on RNA extracts from isolated and purified hepatocytes from 6-to-12-week-old mice confirmed deletion of *Traf2* and *Casp8* in primary hepatocytes from LPC$^{\Delta Traf2,\ Casp8}$ mice (Figure S2M). Finally, LPC$^{\Delta Traf2,\ Casp8}$ livers displayed increased cell proliferation (Figures 1F–1H). Collectively, co-deletion of *Traf2* and *Casp8* in LPC correlated with remodeling of the hepatobiliary architecture featuring massive inflammation, fibrosis, and liver-parenchymal-cell proliferation.

Chronic activation of the necroptosis pathway in LPC$^{\Delta Traf2,\ Casp8}$ mice drives hepatocarcinogenesis

At 52 weeks of age, all LPC$^{\Delta Traf2,\ Casp8}$ mice (13/13) but none of the LPC$^{\Delta Traf2}$ (0/6) or WT (0/9) mice showed multiple hepatic tumors (Table S1) and increased liver-to-body-weight ratios (Figure 2A) as signs of malignancy. Histologically, these tumors displayed characteristic features of HCC as demonstrated by H&E, loss of collagen type IV, and increased GP73 staining (Figures 2B and 2C). To test if cancer development in LPC$^{\Delta Traf2,\ Casp8}$ mice was mediated by necroptosis, we interbred LPC$^{\Delta Traf2,\ Casp8}$ mice with *Ripk3*$^{-/-}$ animals (LPC$^{\Delta Traf2,\ Casp8}$-*Ripk3*$^{-/-}$ mice) (Figure S2N). Of note, LPC$^{\Delta Traf2,\ Casp8}$-*Ripk3*$^{-/-}$ mice did not show signs of tumor development at the age of 52 weeks (0/11) (Figure 2D; Table S1). We additionally performed array-CGH analysis[23] on histologically microdissected liver tumors from LPC$^{\Delta Traf2,\ Casp8}$ mice and compared the patterns of chromosomal aberrations with areas of disturbed microarchitecture in LPC$^{\Delta Traf2}$ and LPC$^{\Delta Traf2,\ Casp8}$-*Ripk3*$^{-/-}$ mice (Figure 2E). This analysis revealed that HCC from LPC$^{\Delta Traf2,\ Casp8}$ mice displayed multiple genetic gains and losses, while no genetic alterations were detected in livers of LPC$^{\Delta Traf2}$ and LPC$^{\Delta Traf2,\ Casp8}$-*Ripk3*$^{-/-}$ mice. To confirm that necroptotic signaling in LPC was the driver of the cancer phenotype in LPC$^{\Delta Traf2,\ Casp8}$

(B) IHC analyses of RIPK3 on liver-tissue sections from 6-week-old mice. Scale bars: 200 and 25 μm for magnifications.
(C) H/E, Sirius red (sRed), and IHC analyses of SOX9, pan-cytokeratin (panCK), αSMA, A6, F4/80, CD3, and B220 on liver-tissue sections from 6-week-old mice. Scale bars: 50 μm.
(D) 3D reconstruction of the biliary system through serial stainings with antibodies against CK19 on liver sections from 6-week-old mice. Scale bars: 100 and 20 μm for magnifications.
(E) Serum analysis of bilirubin and AP in 6-week-old mice. Results are shown as mean, (n = 8), n.s.: not significant.
(F and G) IHC analysis of Ki67 on liver-tissue sections from 6-week-old mice. Scale bar, 50 μm.
(H) Immunoblot analysis of whole-liver protein extracts from 6-week-old mice.
**p < 0.01, ***p < 0.001, ****p < 0.0001; ordinary one-way ANOVA with Tukey's multiple-comparisons test or Kruska-Wallis test with Dunn's multiple-comparisons test, respectively.
See also Figures S1 and S2.

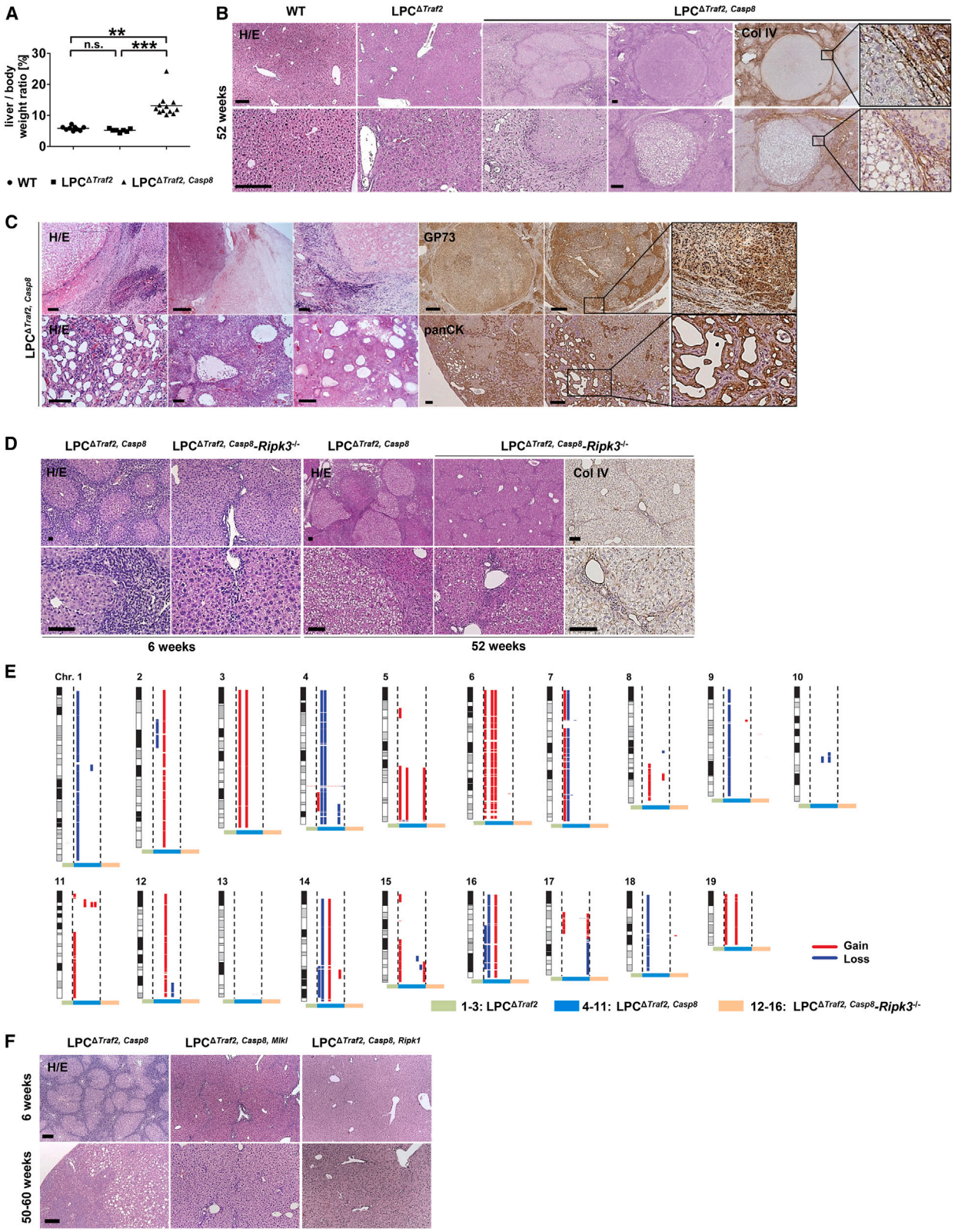

Figure 2. Chronic activation of the necrosome in LPC$^{\Delta Traf2,\ Casp8}$ mice drives liver cancer formation

(A) Liver to body-weight ratios were measured in 50-to-55-week-old mice; n = 9 (WT), n = 7 (LPC$^{\Delta Traf2}$), and n = 12 (LPC$^{\Delta Traf2,\ Casp8}$). Results are shown as mean.

(B) H/E and Col-IV stainings showing liver tumors in 52-week-old LPC$^{\Delta Traf2,\ Casp8}$ mice and no abnormalities in age-matched WT mice. Scale bars: 250 μm.

(legend continued on next page)

mice, we crossed LPC$^{\Delta Traf2,\ Casp8}$ mice with *Mlkl*-floxed mice (LPC$^{\Delta Traf2,\ Casp8,\ Mlkl}$ mice) as well as *Ripk1*-floxed mice (LPC$^{\Delta Traf2,\ Casp8,\ Ripk1}$ mice)[21] (Figure S2N). Of note, additional *Mlkl* deletion as well as *Ripk1* deletion led to a similar rescue of the LPC$^{\Delta Traf2,\ Casp8}$ phenotype as shown for *Ripk3* deletion (Figure 2F; Table S1). Together, these findings suggested that RIPK1-RIPK3-MLKL-dependent necroptosis signaling promoted hepatocarcinogenesis in LPC$^{\Delta Traf2,\ Casp8}$ mice.

NF-κB-activation is a prerequisite for necroptotic hepatocarcinogenesis

The fact that RIPK3 promoted inflammation and hepatocarcinogenesis in LPC$^{\Delta Traf2,\ Casp8}$ mice conflicted with our previous findings in mice with genetic ablation of the kinase *Tak1* in LPC (LPC$^{\Delta Tak1}$),[24] in which RIPK3 inhibited hepatocarcinogenesis due to an unknown mechanism.[16] TAK1 is required to activate the catalytic IKK subunits,[25] and LPCs lacking *Tak1* display a complete block of NF-κB activation.[24,26] By contrast, it has been previously shown that TRAF2 deletion in mouse embryonic fibroblasts (MEFs) resulted in constitutive hyperactivation of NF-κB.[27] We confirmed basal and inducible NF-κB hyper-activation in livers and primary hepatocytes from LPC$^{\Delta Traf2}$ mice by electrophoretic mobility shift assay (EMSA) (Figures S3A and S3B). Therefore, we hypothesized that the activation status of the IKK complex and the NF-κB pathway might determine if RIPK3-dependent necroptosis is pro- or antitumorigenic.

To test this hypothesis, we crossed LPC$^{\Delta Traf2,\ Casp8}$ mice with *Ikbkb*-floxed (*Ikk*β) mice to generate LPC$^{\Delta Traf2,\ Casp8,\ Ikbkb}$ mice (Figure S3C). As expected, additional deletion of *Ikk*β abrogated spontaneous and TNF-induced NF-κB activation in primary hepatocytes from LPC$^{\Delta Traf2,\ Casp8}$ mice, as demonstrated by EMSA (Figure 3A) and by expression analysis for the NF-κB target gene *A20* in whole liver extracts (Figures 3B and 3C). Additional ablation of *Ikk*β rescued the ductular-reaction phenotype seen in 6-week-old LPC$^{\Delta Traf2,\ Casp8}$ mice (Figure 3D). However, young LPC$^{\Delta Traf2,\ Casp8,\ Ikbkb}$ mice showed the presence of focal hepatocellular necrotic lesions (Figure 3D). These necrotic lesions went along with rising liver enzymes as a surrogate for increased liver injury, but reduced cholestasis parameters (Figure S3D). Of note, liver tumors were not detected in 52-week-old LPC$^{\Delta Traf2,\ Casp8,\ Ikbkb}$ mice (0/11) (Figure 3D; Table S1). However, array-CGH analysis on microdissected, histologically disturbed areas from old LPC$^{\Delta Traf2,\ Casp8,\ Ikbkb}$ mice showed that chromosomal aberrations could still be detected, but to a lesser extent than those seen in tumors from LPC$^{\Delta Traf2,\ Casp8}$ mice (Figure 3E).

IKKs were implicated in the modulation of RIP kinase activity in an NF-κB-independent manner.[7,28,29] Therefore, to exclude that an NF-κB independent function of IKKβ mediated the phenotype of LPC$^{\Delta Traf2,\ Casp8}$ mice, we inhibited NF-κB through alternative targeting approaches. Additional ablation of the regulatory IKK subunit *Nemo* (LPC$^{\Delta Traf2,\ Casp8,\ Ikbkg}$) or the NF-κB subunit *Rela* (*p65*) (LPC$^{\Delta Traf2,\ Casp8,\ Rela}$) resulted in a similar rescue of the phenotype as seen upon additional *Ikk*β ablation (Figures 3F and S3E; Table S1), arguing for a crucial function of NF-κB signaling and against an NF-κB-independent effect of IKKβ in the mediation of necroptotic carcinogenesis in LPC$^{\Delta Traf2,\ Casp8}$ mice. Of note, all additional genetic constellations of spontaneous necroptosis activation in a setting of NF-κB inhibition (LPC$^{\Delta Ikbkg,\ Casp8}$, LPC$^{\Delta Tak1,\ Casp8}$) displayed similar necrosis areas as previously detected in LPC$^{\Delta Traf2,\ Casp8,\ Ikbkb}$ mice but were rescued from cancer development (Figure S3F).

As impaired TRAF2 signaling is also known to be related to activation of noncanonical NF-κB signaling,[30,31] we tested p100 expression and cleavage to p52 by immunoblot in primary hepatocytes and liver extracts. Cleavage to the p52 form was induced in hepatocytes and livers of LPC$^{\Delta Traf2,\ Casp8}$ and LPC$^{\Delta Traf2,\ Casp8}$-*Ripk3*$^{-/-}$ mice but not in WT mice (Figure 3G). Moreover, additional deletion of *Ikk*β abolished the expression of p100, resulting in the absence of the p52 cleavage form in these mice (Figure 3G). This finding confirmed the functional interconnection between canonical and noncanonical NF-κB signaling.[32] Collectively, these results showed that inactivation of NF-κB in hepatocytes with activated necroptosis resulted in the formation of necrotic foci that did not progress to HCC. By contrast, hyperactivation of NF-κB in hepatocytes with activated necroptosis signaling promoted hyperproliferation and HCC development.

An NF-κB necroptosis signature predicts clinical outcome of liver cancer patients

We aimed at providing evidence that combined NF-κB and necroptosis signaling might influence the prognosis of human HCC. Similar to mice, we confirmed low RIPK3 expression in hepatocytes from healthy liver tissue as well as in liver tissue from NASH patients by ISH analysis (Figure S3G). Next, we compared the gene expression profiles of murine LPC$^{\Delta Traf2,\ Casp8}$ liver tumors with human HCCs. For this, we first performed an RNA-sequencing analysis in tumors from 52-week-old LPC$^{\Delta Traf2,\ Casp8}$ mice. Unsupervised clustering of expression data discriminated LPC$^{\Delta Traf2,\ Casp8}$ tumors from nontumoral liver tissue (Figure 4A). Differential gene expression (Figure 4B; Table S2) showed upregulation of genes whose human orthologs are recurrently upregulated in HCC patients[33,34] (Figure 4C). As predicted, gene set enrichment analysis (GSEA) showed significant enrichment of gene sets related to cell-cycle, proliferation, inflammation, and

(C) H/E and IHC (GP73, panCK) analysis on liver paraffin sections from 52-week-old LPC$^{\Delta Traf2,\ Casp8}$ mice indicating HCC development. Scale bars: 100 μm for H/E and panCK; 500 μm for GP73.
(D) H/E and Col-IV stainings showing a rescue of liver pathology by additional deletion of *Ripk3* in LPC$^{\Delta Traf2,\ Casp8}$ mice. Scale bars: 100 μm.
(E) Summary of comparative genomic hybridization (CGH) analysis from different hepatic tumors of LPC$^{\Delta Traf2,\ Casp8}$ mice (n = 8) and samples of areas with disturbed histological architecture (no obvious tumors) from LPC$^{\Delta Traf2}$ (n = 3) and LPC$^{\Delta Traf2,\ Casp8}$-*Ripk3*$^{-/-}$ mice (n = 5) (50-to-55-week old). The q-arm of each chromosome is shown and chromosome numbers are indicated. Dark horizontal bars within the symbolized chromosomes represent G bands. Chromosomal deletions are indicated in blue, amplifications in red. Individual mice are labeled by horizontal collared bars.
(F) H/E of livers from 6-week-old mice. Scale bars: 200 μm.
**p < 0.01, ***p < 0.001. n.s., not significant; Kruska-Wallis test with Dunn's multiple-comparisons test.
See also Figure S2 and Table S1.

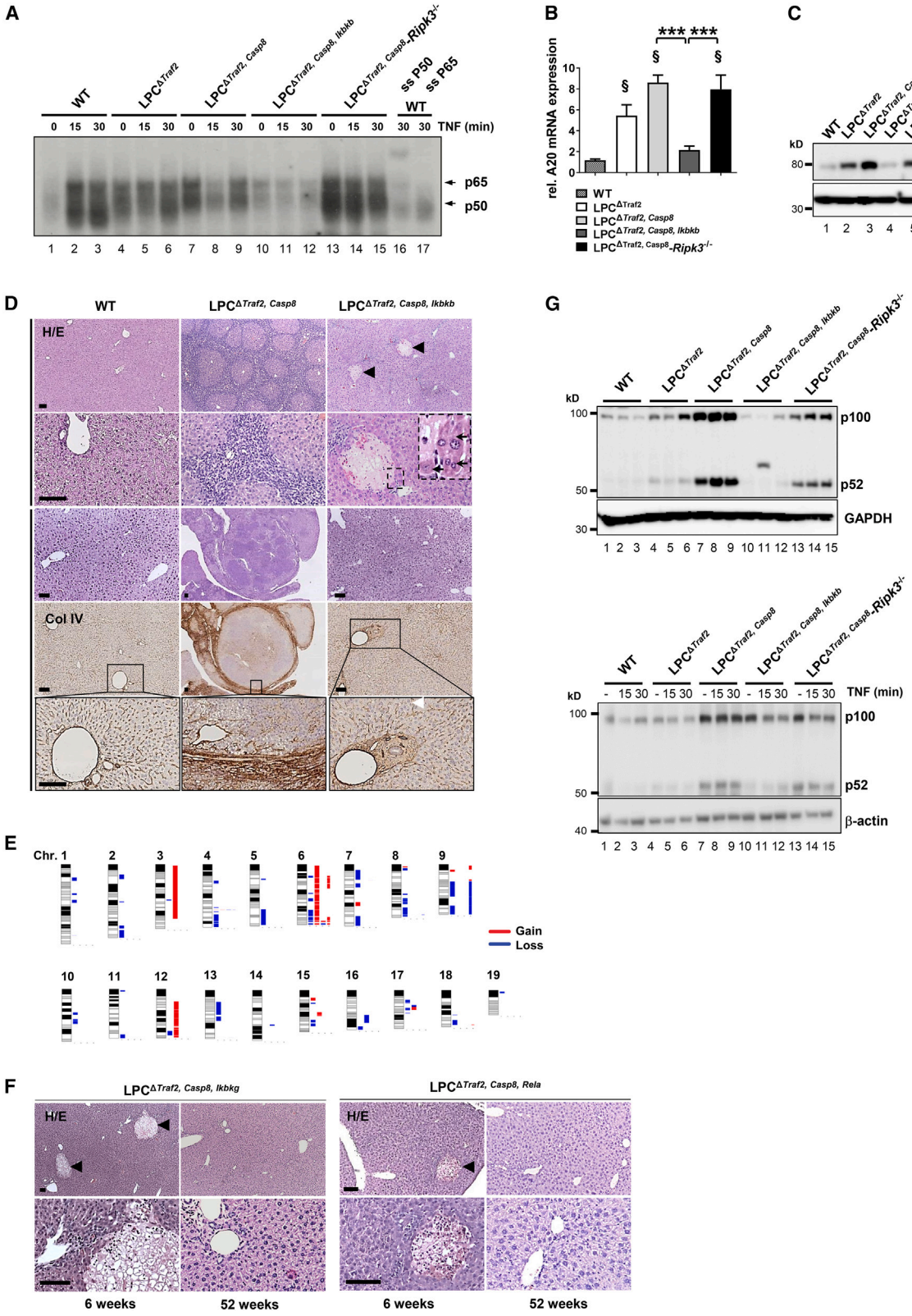

Figure 3. NF-κB-activation is a gatekeeper for necroptotic hepatocarcinogenesis

(A) NF-κB inactivation through the additional deletion of *Ikk*β in LPC$^{\Delta Traf2,\ Casp8}$ mice was shown by EMSA from nuclear protein extracts from isolated and TNF (20 ng/mL)-treated primary hepatocytes.

(legend continued on next page)

NF-κB signaling (Table S2). Liver cancer signatures associated with aggressive clinical behavior in humans such as the *Proliferation*-[35] or *S1*-subclasses[36] were also significantly enriched in LPC$^{\Delta Traf2,\ Casp8}$ tumors (Table S2).

We next applied comparative functional genomics and generated an "NF-κB necroptosis signature" from the LPC$^{\Delta Traf2,\ Casp8}$ tumors (Table S2). Performance of the signature was tested in a cohort of tumor samples from 228 HCC patients treated with surgical resection.[42] A total of 20/228 (8.7%) patients were predicted with the NF-κB necroptosis signature (nearest template prediction [NTP] method, FDR < 0.05) (Figure 4D). These patients were also enriched in previously reported signatures associated with aggressive tumors,[38] including the *Proliferation* and *S1-subclasses*, both also enriched in the LPC$^{\Delta Traf2,\ Casp8}$ tumors (Fisher exact test, $p < 0.05$) (Figure 4D). Other signatures associated with biliary-precursor cell phenotypes such as the *CK19-hum*,[38] *CK19-rat*,[39] or *Notch* signatures[40] were also significantly enriched in patients with the NF-κB necroptosis signature (Figure 4D). Moreover, mRNA-expression of the necroptosis executor *MLKL* was higher in these patients (Mann-Whitney U, $p = 0.0006$) compared with those without the signature (Figure 4D). In terms of clinical outcomes, patients with the NF-κB necroptosis signature had significantly higher rates of early tumor recurrence (<2 years after resection, $p < 0.05$) (Figure 4E). Taken together, these data indicate that murine LPC$^{\Delta Traf2,\ Casp8}$ tumors show transcriptional features resembling aggressive human HCC, suggesting that the activation of NF-κB and necroptosis signaling represents a risk factor for an unfavorable outcome of patients with liver cancer.

Necrosome activation is a prerequisite for chemokine and cytokine release from NF-κB-activated parenchymal cells

We aimed at further dissecting the molecular mechanisms linking necrosome activation in LPC with NF-κB activation and hepatocarcinogenesis. We hypothesized that NF-κB might induce transcription of inflammatory factors (cytokines and chemokines) in hepatocytes, which might subsequently be released from these cells through activation of necroptosis. We first performed a transcriptional micro-array analysis on whole-liver RNA extracts from 7-day-old mice because, at this age, the phenotype was not yet fully established, therefore increasing the likelihood to detect hepatocyte-specific transcriptional patterns. As illustrated by heatmap analysis, LPC$^{\Delta Traf2,\ Casp8}$ and LPC$^{\Delta Traf2,\ Casp8}$-*Ripk3*$^{-/-}$ livers showed a similar expression pattern at this age that was distinct from LPC$^{\Delta Traf2,\ Casp8,\ Ikbkb}$ livers (Figure 5A), indicating an NF-κB-driven expression profile in hepatocytes from LPC$^{\Delta Traf2,\ Casp8}$ mice.

Among the lists of genes with more than 2-fold upregulation in LPC$^{\Delta Traf2,\ Casp8}$ and LPC$^{\Delta Traf2,\ Casp8}$-*Ripk3*$^{-/-}$ livers (with activated parenchymal NF-κB signaling) that were not upregulated in LPC$^{\Delta Traf2,\ Casp8,\ Ikbkb}$ mice (Table S3), we identified *Ccl20*, a known proinflammatory and procarcinogenic cytokine.[43] RT-qPCR and IHC analyses confirmed *Ccl20* upregulation in LPC$^{\Delta Traf2,\ Casp8}$ and LPC$^{\Delta Traf2,\ Casp8}$-*Ripk3*$^{-/-}$ livers at the age of 6 weeks with strong protein expression in LPCs, which was nearly absent in LPC$^{\Delta Traf2,\ Casp8,\ Ikbkb}$ livers (Figures 5B–5D). To further test the hypothesis that despite transcriptional upregulation, CCL20 would not be released from LPC if necroptosis is blocked in LPC$^{\Delta Traf2,\ Casp8}$-*Ripk3*$^{-/-}$ livers, we measured CCL20 concentrations in the serum of 6-week-old mice. This analysis revealed that CCL20 was only elevated in the serum of LPC$^{\Delta Traf2,\ Casp8}$ mice, in which NF-κB and necroptosis were both active (Figure 5E). Further analysis of known NF-κB-dependent mitogenic and inflammatory cytokines by multiplex enzyme-linked immunosorbent assay (ELISA) in 6-week-old mice revealed that in addition to CCL20, also IL-6, MCP-1, and TNF were also released into the serum of LPC$^{\Delta Traf2,\ Casp8}$, but not in LPC$^{\Delta Traf2,\ Casp8,\ Ikbkb}$ and LPC$^{\Delta Traf2,\ Casp8}$-*Ripk3*$^{-/-}$ or LPC$^{\Delta Traf2,\ Casp8,\ Ripk1}$ mice (Figure 5F).

To provide further evidence for our hypothesis of a common function of NF-κB- and necrosome activation in the process of chemokine expression and release, we treated *Traf2*$^{-/-}$ MEFs with the necroptosis activating caspase-inhibitor zVAD (Figure 5G) to phenocopy LPC$^{\Delta Traf2,\ Casp8}$ mice. EMSA of WT and *Traf2*$^{-/-}$ MEFs confirmed spontaneous NF-κB activation in TRAF2-deficient MEFs (Figure 5H). RT-qPCR-analysis on lysates from these cells showed that TNF treatment strongly induced *Ccl20, Mcp1* and *Il6* mRNA expression in these cells. In the case of *Ccl20*, the effect was partially abolished by RIPK1 inhibition (Nec1 treatment), while NF-κB inhibition (TPCA treatment) resulted in suppression of *Ccl20*, *Mcp1*, and *Il6* expression (Figure S3H). Consistently, an ELISA on supernatants revealed that TNF treatment resulted in MCP-1 and IL-6 release only in conditions of NF-κB and simultaneous necroptosis, whereas either inhibition of RIPK1 (Nec-1), NF-κB (TPCA) or combined cell-death inhibition (zVad and Nec-1 [ZN]) fully inhibited cytokine release from these cells to the supernatants (Figure 5G). Finally, we analyzed etanercept- and vehicle-treated mice (Figures S3I and S3J) and found no effect on inflammation and proliferation, but a downregulation of IL-6 and a partial

(B) qRT-PCR analysis of *A20* mRNA expression (n = 6) in livers of 6-week-old mice. All values were normalized to β-actin expression. Results are expressed as mean with SEM.

(C) Immunoblot analysis of the NF-κB target gene A20 on whole-liver protein extracts from the indicated mice.

(D) H/E and Col-IV staining showing loss of tumor formation in 52-week-old LPC$^{\Delta Traf2,\ Casp8,\ Ikbkb}$ mice but the appearance of necrotic foci surrounded by hypereosinophilic hepatocytes (black arrows) in 6-week-old mice (black arrowhead) and mild periductal fibrosis in 52-week-old mice (white arrowhead). Scale bars: 100 μm.

(E) Summary of CGH analysis on microdissected areas with disturbed histological architecture (no obvious tumors) in 4x LPC$^{\Delta Traf2,\ Casp8,\ Ikbkb}$ (48-to-52-week-old) mice, showing several chromosomal aberrations without the presence of HCCs. Chromosomal deletions are indicated in blue and amplifications in red.

(F) Histological rescue of the observed phenotype seen in 6-week and 52-week-old LPC$^{\Delta Traf2,\ Casp8}$ mice by additional deletion of either *Nemo* or *RelA* were associated with the appearance of necrotic foci (black arrowheads). Scale bars: 100μm.

(G) Immunoblot analysis of whole-liver protein extracts from 6-week-old mice) (upper panel) and protein extracts from primary, TNF-treated hepatocytes from 6 to 12-week-old mice (lower panel).

Results are expressed as mean with SEM. ***$p < 0.001$; §, significantly different compared with WT.

See also Figure S3 and Table S1.

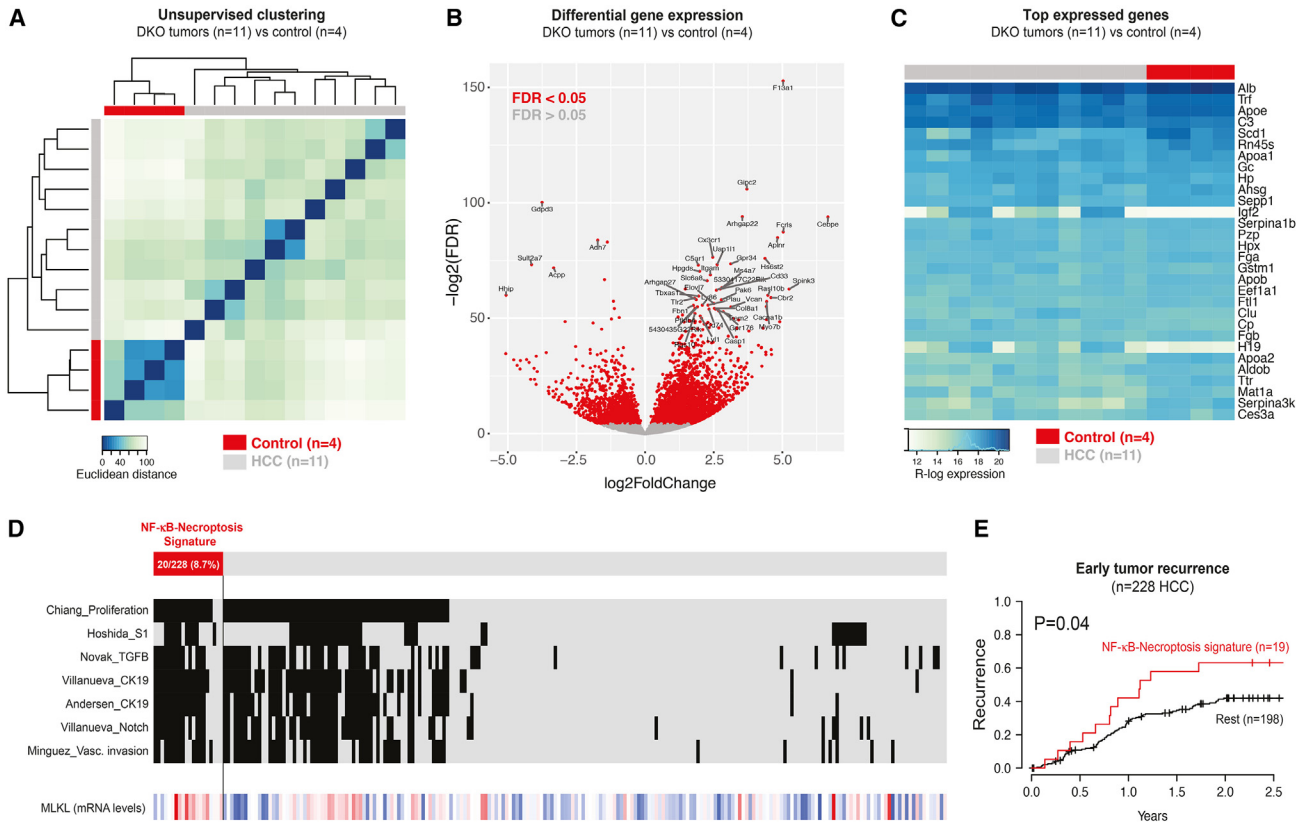

Figure 4. An NF-κB necroptosis signature predicts clinical outcome of liver cancer patients

(A) Unsupervised clustering of RNA-seq data of LPC$^{\Delta Traf2,\ Casp8}$ tumors (n = 11, 50–55-weeks old) and unaffected control tissue (LPC$^{\Delta Traf2,\ Casp8}$-*Ripk3*$^{-/-}$), n = 4, 50-to-54-weeks old).

(B) Volcano plot of differentially expressed genes between LPC$^{\Delta Traf2,\ Casp8}$ tumors (n = 11) and control tissue (n = 4). x axis represents magnitude of the difference as determined by $\log_2$ fold change; y axis measures significance using $\log_2$ FDR. Red dots show genes which are differentially expressed with FDR < 0.05 (tumor versus control).

(C) Top expressed genes in the LPC$^{\Delta Traf2,\ Casp8}$ tumors (n = 11) and control (n = 4).

(D) Human HCC samples with a positive prediction for the NF-κB necroptosis gene signature as determined by the NTP method (red bars). Predictions for previously reported gene signatures are overlapped below (black bars). All listed are significantly enriched (Fisher exact test) in patients with the NF-κB necroptosis signature including: proliferation[35] (P = 3E-6), S1[36] (P = 1E-4), late TGF-β[37] (P = 2E-4), CK19-human[38] (P = 4E-6), CK-rat[39] (P = 6E-6), Notch[40] (P = 3E-4) and Vascular Invasion[41] (P = 2E-4).

(E) Kaplan-Meier curve for early tumor recurrence (<2 years following resection). Patients with the NF-κB necroptosis gene signature (n = 19) are shown in red. The analysis included all patients from (E) for which survival data were available.

See also Figure S3 and Table S2.

decrease of MCP-1 in the serum of etanercept-treated LPC$^{\Delta Traf2,\ Casp8}$ mice (Figure S3K). By contrast, CCL20 serum concentrations were slightly increased, indicating that TNF-dependent and -independent mediators contributed to the phenotype observed in LPC$^{\Delta Traf2,\ Casp8}$ mice.

Together, these findings indicated that NF-κB activation was able to drive the expression of chemokines in hepatocytes and MEFs while activation of the necrosome facilitated the release of these respective factors.

Activation of NF-κB and the necrosome synergistically trigger hepatic infiltration with a profibrotic and procarcinogenic subset of monocyte-derived macrophages

We next examined how this molecular mechanism of cytokine release related to the infiltration of specific immune-cell subsets that might contribute to fibrosis and cancer. IHC stainings revealed an increase of F4/80$^+$ and CD3$^+$ immune cells in LPC$^{\Delta Traf2,\ Casp8}$ livers (Figures S4A and S4B). By contrast, immune-cell infiltrates in LPC$^{\Delta Traf2,\ Casp8,\ Ikbkb}$ mice were spatially enriched in the focal areas of LPC necrosis (Figure S4C). To further characterize specific immune-cell subsets, we performed a single-cell RNA-sequencing analysis on CD45$^+$CD31$^-$-FACS-sorted immune cells from 6-to-10-week-old WT, LPC$^{\Delta Traf2,\ Casp8}$, LPC$^{\Delta Traf2,\ Casp8}$-*Ripk3*$^{-/-}$, and LPC$^{\Delta Traf2,\ Casp8,\ Ikbkb}$ livers. Based on their expression profiles, we identified 17 distinct clusters (Figure 6A). Specific subsets of monocyte-derived macrophages (MoMFs) and neutrophils were found enriched in LPC$^{\Delta Traf2,\ Casp8}$ mice (Figures 6A and 6B). A further subclustering analysis showed distinctly enriched subclusters of MoMFs I and II in LPC$^{\Delta Traf2,\ Casp8}$ mice, while the numbers of MoMF III and especially Kupffer

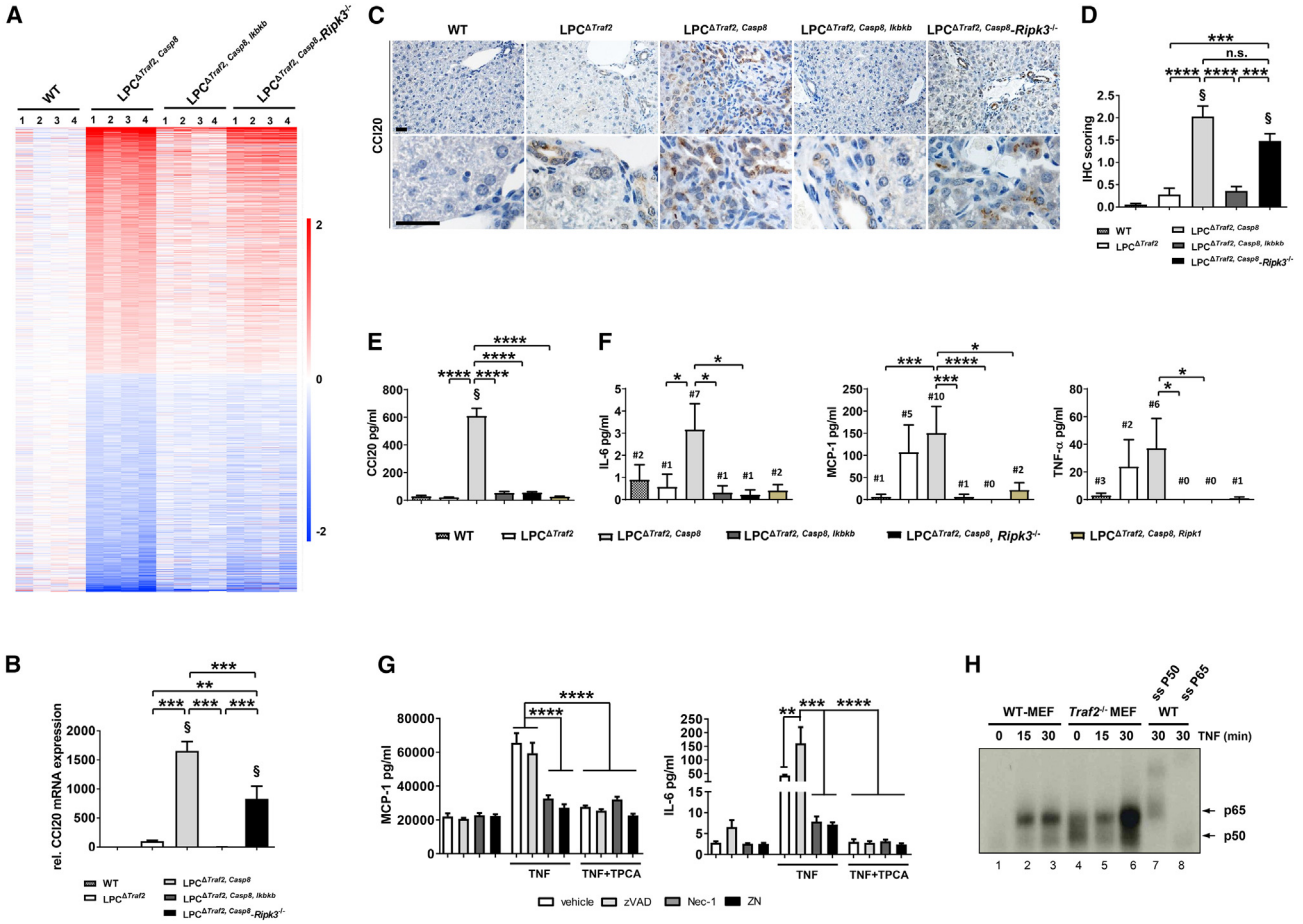

Figure 5. Necrosome activation is a prerequisite for cytokine and chemokine release from NF-κB-activated hepatocytes

(A) Microarray analysis (heatmap) of whole-liver RNA extracts from 7-day old mice (n = 4).

(B) qRT-qPCR analysis of *CCL20* mRNA expression (n = 6) in livers of 6-week-old mice. All values were normalized to β-actin expression. Results are expressed as mean with SEM.

(C and D) IHC and statistical analysis for CCL20 on liver paraffin sections from 6-week-old mice. Results are shown as mean with SEM, n = 5, n.s.: not significant, (0 = negative; 1 = weak; 2 = moderate; 3 = strong). Scale bars: 100 μm.

(E) CCL20 serum concentrations in the respective mice were analyzed by ELISA. Results are shown as mean with SEM (n = 7–8).

(F) Serum concentrations of MCP-1, IL-6, and TNF in the depicted mice (n = 10) were assessed by BioPlex Assay. The numbers of mice with detectable serum concentrations are indicated. Results are shown as mean with SEM.

(G) Concentrations of MCP-1 and IL-6 in the supernatant of TNF-treated (50 ng/mL) *Traf2*$^{-/-}$ MEF cells in the presence of zVAD-fmk (20 μM), Nec-1 (10 μM), and TPCA (20 μM) were assessed by BioPlex Assay. Results are shown as mean with SEM and represent three technical replicates. Basal NF-κB hyperactivation in *Traf2*$^{-/-}$ MEF cells is shown by EMSA from nuclear protein extracts from TNF (50 ng/mL)-treated cells. ****p < 0.0001, ***p < 0.001, **p < 0.01, *p < 0.05; §, significantly different compared with WT. Ordinary one-way ANOVA with Tukey's multiple-comparisons test or Kruska-Wallis test with Dunn's multiple-comparisons test, respectively.

cells (KCs) were decreased compared with all other genotypes (Figure 6C). The subpopulations MoMF I and MoMF II in LPC$^{\Delta Traf2,\ Casp8}$ mice showed an increased expression of *Tnf* and *Mcp1* (Figure S4D). *Il6*, on the other hand, was mainly found expressed in KCs while *Ccl20* was not found expressed in MoMFs or in KCs (Figure S4D). A further unsupervised hierarchical clustering analysis revealed a specific gene signature observed in MoMFs I and II but not in MoMF III and KCs that was previously associated with profibrotic macrophages in lung fibrosis of mice and humans[44] (Figures 6D and 6E). Moreover, several genes upregulated in MoMFs I and II were previously found upregulated in procarcinogenic macrophages[45–47] (Figures 6D and 6E).

To further test the contribution of monocytes and macrophages to the LPC$^{\Delta Traf2,\ Casp8}$ phenotype, we treated LPC$^{\Delta Traf2,\ Casp8}$ mice with clodronate-loaded liposomes as well as PBS-loaded liposomes as controls. Efficient depletion of F4/80^{+} MoMFs was confirmed by IHC, qRT-PCR, and immunoblot analyses (Figures S5A–S5D). At the transcriptional level, MoMF depletion did not alter *Ccl20* expression but showed a trend toward lower expression for *Mcp1, Tnf*, and *Il6* (Figure S5D). These data were in line with our single-cell RNA-sequencing data (Figure S4D), suggesting that CCL20 is one exemplary chemokine that was primarily secreted from hepatocytes. By contrast, MCP1 and, to a greater extent, TNF and IL-6 were partially or primarily secreted by MoMFs, augmenting

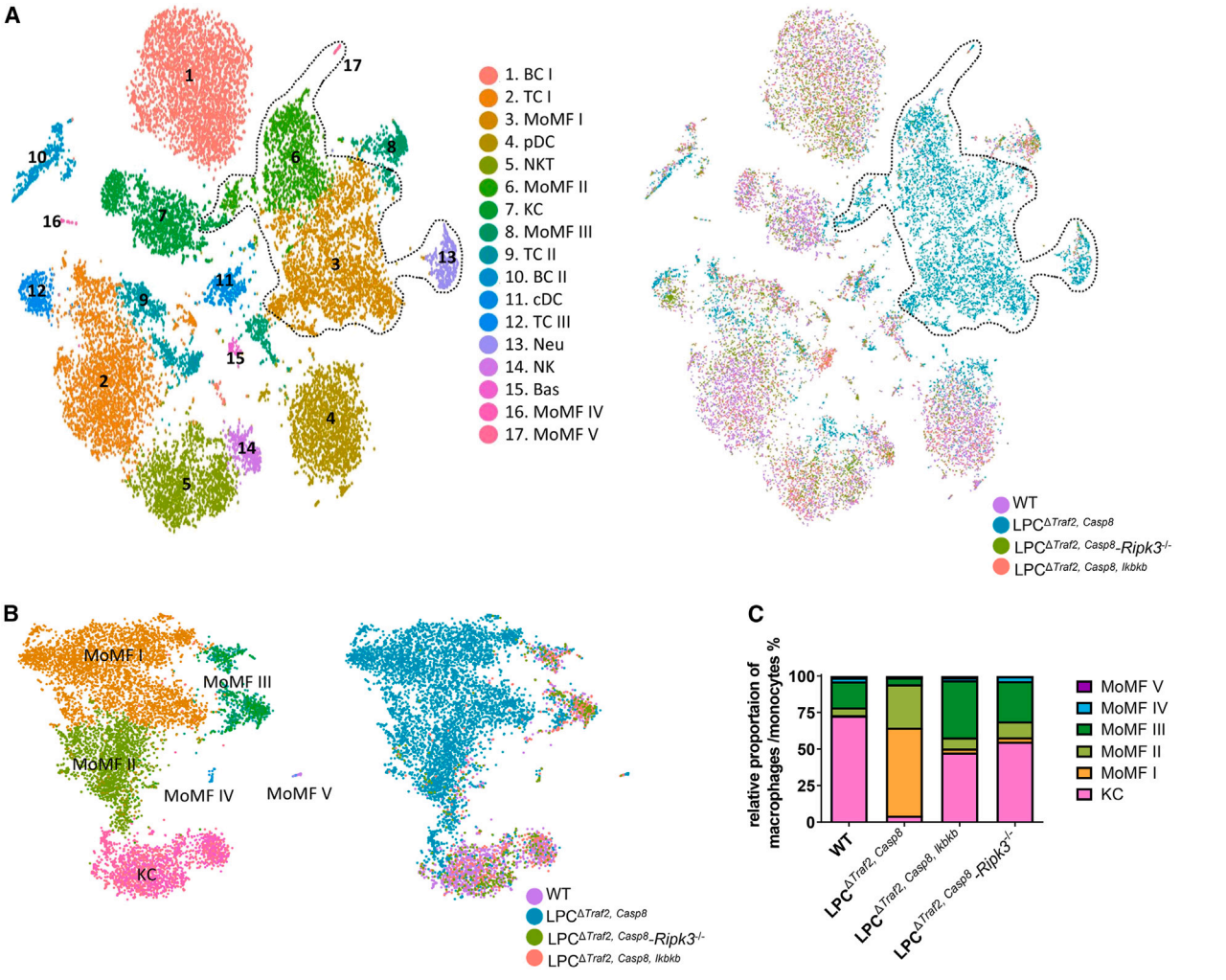

(legend on next page)

an inflammatory response promoting and amplifying carcinogenesis in LPC$^{\Delta Traf2,\ Casp8}$ livers.

NF-κB activation forces necroptotic hepatocytes into a sublethal state *in vivo*

While we showed that necrosome activation is a prerequisite for NF-κB-dependent cytokine and chemokine release from hepatocytes, it had remained unclear whether this necrosome activation was equivalent to a complete execution of cell death or whether alarmins were released without leading to complete cell death. To answer this question *in vivo*, we applied functional intravital two-photon-microscopy using vital dyes enabling us to correlate membrane leakiness (propidium iodide [PI], SYTOX Green, and Texas Red-coupled dextran) with markers indicating loss of mitochondrial potential (MP) (rhodamine123 or tetramethylrhodamine, ethyl ester [TMRE]) as a cellular event closely preceding cell-death execution.[48,49]

To establish this method, we first analyzed necrotic areas in LPC$^{\Delta Traf2,\ Casp8,\ Ikbkb}$ livers. LPCs in these areas were strongly positive for PI and lost their MP (Figure S5), and moreover showed morphological features indicating full execution of cell death *in vivo* (Video S1). By contrast, a similar analysis in LPC$^{\Delta Traf2,\ Casp8}$ livers showed high numbers of PI-positive hepatocytes that maintained their MP (Figure 7A; Video S2), suggesting the presence of hepatocytes with active energy metabolism but with leaky membranes. As expected, no cell-death-related events were detected in WT and LPC$^{\Delta Traf2,\ Casp8}$-*Ripk3*$^{-/-}$ mice (Figure 7A). These results were corroborated using chemically distinct but functionally comparable intravital dyes, namely SYTOX Green as an alternative dye indicating membrane leakiness and TMRE as a functional marker of MP (Figure S5S; Videos S3 and S4). In an alternative approach, we repetitively injected LPC$^{\Delta Traf2,\ Casp8}$ mice with Texas Red-coupled dextran (3000 Da) (Video S5; Figures 7B and 7C). This analysis revealed that leaky hepatocytes in LPC$^{\Delta Traf2,\ Casp8}$ livers showed a fast increase in intracellular dextran intensity but a fast decrease to initial intensity, suggesting a bidirectional permeability of these leaky membranes for larger molecules (Figure 7B; Video S5). Moreover, analysis of PI (nuclear)- and dextran (cytoplasmic)-associated fluorescence in the same hepatocytes showed a strong correlation, demonstrating that the membranes of PI-positive hepatocytes were also permeable to the larger molecule dextran (Figure 7C).

We further characterized the kinetics of cell-membrane leakiness versus. The loss of MP for periods up to ∼400 min (Figures 7D–7G; Videos S1 and S2). In LPC$^{\Delta Traf2,\ Casp8,\ Ikbkb}$ mice, the time interval between the occurrence of membrane leakage until loss of MP was very short, averaging 32.0 min (23.2–40.8) (median, 95%-CI) in a Kaplan Meier analysis (Figures 7D, 7F, and 7G; Video S1). By contrast, only few hepatocytes were found in the LPC$^{\Delta Traf2,\ Casp8}$ livers that had both a leaky cell membrane and lost MP (Figures 7D and 7E; Video S5), which indicates that cell death was fully executed only in few hepatocytes within a given time interval. By contrast, a Kaplan-Meier analysis showed that the majority of hepatocytes remained in a sublethal, "undead" state (leaky membrane, active MP) for more than 400 min (maximum observation time) (Figure 7G). Moreover, we correlated images from the intravitally recorded videos with TUNEL analyses from the distinct mouse models and found only very few TUNEL-positive cells in LPC$^{\Delta Traf2,\ Casp8}$ livers compared with the number of "undead" PI-positive hepatocytes (Figures S5E, S5G, and 7A). By contrast, there was a high correlation and overlap between those necrotic foci with all features of cell death as defined in our intravital microscopy analysis (Figure S5E) with the amount of TUNEL-positive cells in LPC$^{\Delta Traf2,\ Casp8,\ Ikbkb}$ livers (Figure S5G).

Finally, to provide evidence that sublethal necrosome activation can be found also in human cells, we reproduced our two-photon-imaging approach in human cultured primary hepatocytes pretreated with TWEAK (to deplete TRAF2) and zVAD (to inhibit caspases), and stimulated them with TNF. Using a similar approach for intravital imaging of mice, we identified human hepatocytes with leaky membranes by SYTOX Green positive nuclei. Only a small fraction of these SYTOX Green-positive hepatocytes still showed an active MP over a period of several hours (Video S6), suggesting that, in general, human hepatocytes can also execute the molecular mechanisms related to sublethal necrosome activation. However, in the majority of cell-death events in human hepatocytes, MP was lost before the nuclei became SYTOX Green positive.

DISCUSSION

The precise fate of a cell with activated MLKL *in vivo* is not yet clear, and little information is available about the kinetics and transition phases between MLKL activation and cell-death execution. In this work, we demonstrated that necrosome activation in hepatocytes *in vivo* can lead to distinct cell-death fates depending on the competence for NF-κB activation, and this can act as a switch either preventing or promoting inflammation and hepatocarcinogenesis. Our detailed kinetic analysis of the execution of necroptosis and its consequences *in vivo* by intravital microscopy showed that pre- or concurrent activation of NF-κB in hepatocytes extended the time span of necroptosis execution, resulting in a sublethal cell state with intact membrane potential but permeable cell membranes that formed the

Figure 6. Activation of NF-κB and the necrosome synergistically trigger hepatic infiltration with a profibrotic and procarcinogenic subset of monocyte-derived macrophages

(A) t-SNE plot mapping the identity of different CD45^{+}CD31^{-} immune cells from the indicated genotypes.

(B) Subset clustering of immune cells after exclusion of contaminating cells from scRNA-seq datasets.

(C) Distribution (%) of Kupffer cells (KC) and MoMF subpopulation (I-V) between the different genotypes.

(D) Heatmap of genes differentially expressed between MoMF I and MoMF II versus KC. Only genes were considered with an average log expression fold-change >1.5 in MoMF I and MoMF II.

(E) Heatmap of genes differentially expressed between MoMF I and MoMF II versus MoMF III genes with fold change >1.5 in both groups were considered. Genes were clustered based on a complete linkage hierarchical cluster.

See also Figures S3–S5.

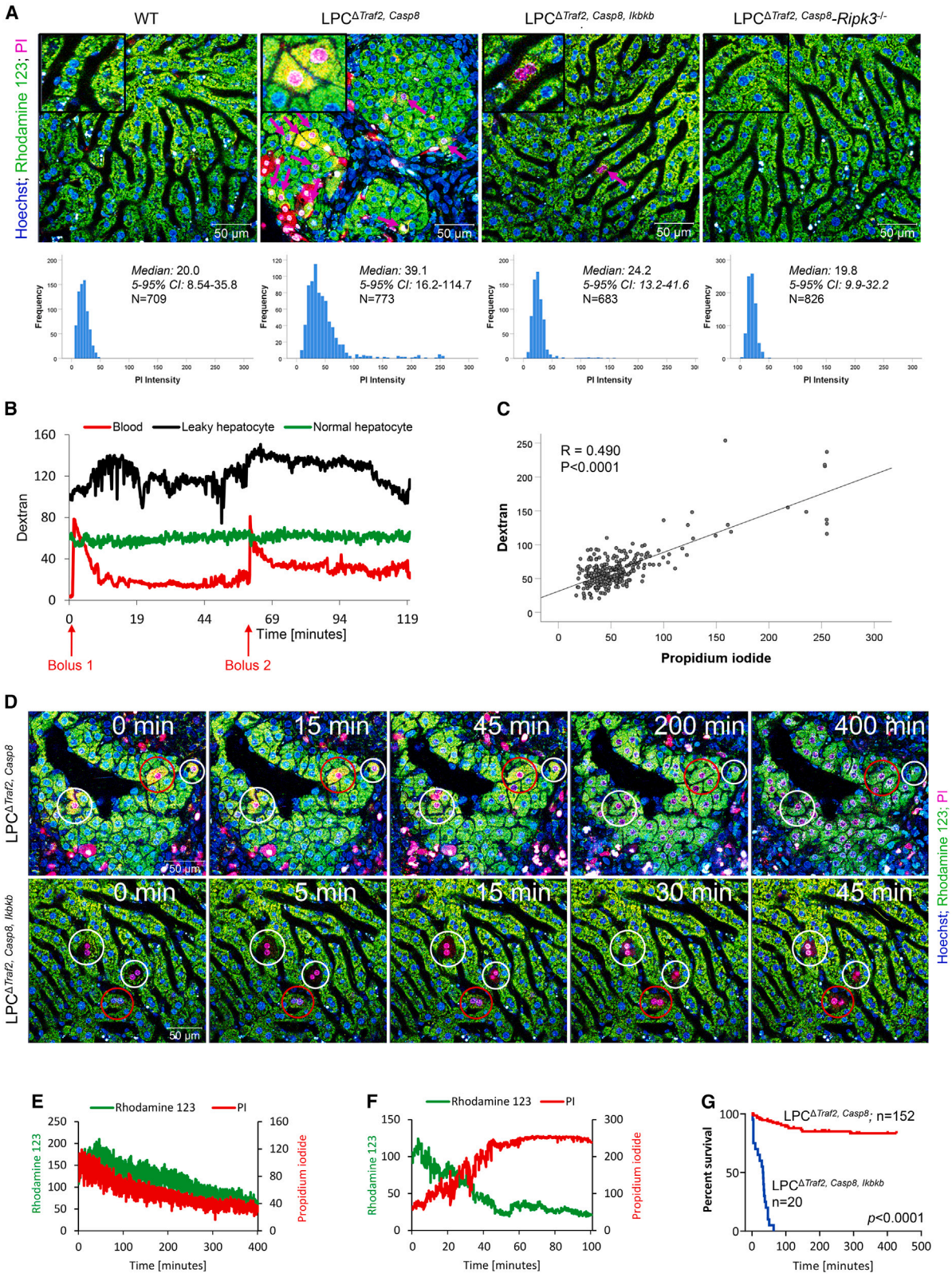

Figure 7. Sublethal necrosome activation of hepatocytes *in vivo* depends on NF-κB

(A) Intensity of nuclear propidium iodide (PI) in the indicated mice. Scale bars: 50 μm. The frequency plots summarize nuclei from 3 to 9 mice per model. Arrows indicate PI-positive hepatocytes with intact mitochondrial membrane potential. Red cells lost their mitochondrial membrane potential. Scale bars, 50 μm.

(legend continued on next page)

basis for releasing mitogenic and inflammatory DAMPs from hepatocytes. How long cell-death execution could be extended *in vivo* through NF-κB activation could not be clarified exactly, as the putative time span exceeded the maximum experimental observation time of 400 min for most analyzed cells with leaky cell membranes.

The concept of "undead" cells secreting mitogenic factors has previously been suggested in *Drosophila*, where artificially blocked apoptosis results in the presence of undead cells with active caspases that stimulated tissue overgrowth by releasing mitogenic factors.[50] In line, a recent study suggested that mammalian cells can undergo limited plasma-membrane damage from the membrane-disrupting action of MLKL, triggering a plasma integrity-sensing pathway involving TAK1, IKKs and RelA and subsequent cytokine and chemokine release.[12] In this study, the authors hypothesized that this pathway may be activated *in vivo* particularly in tumors that tend to downregulate RIPK3, resulting in incomplete MLKL phosphorylation, which is associated with reduced plasma-membrane damage and thus cell survival. The results we present here suggest that naturally low RIPK3 expression in hepatocytes represents a prerequisite for sublethal necroptosis signaling, thus shedding light on the previous controversial discussion of whether hepatocytes can undergo necroptosis or not.[51,52] This could also explain why necrosome activation has not been associated with cancer development in gut or skin originating from epithelial cell compartments with higher RIPK3 expression.[53,54] However, further experiments are warranted to elucidate the exact nature of NF-κB and NF-κB-dependent genes on pore formation and membrane integrity *in vitro* and *in vivo*.

TRAF2-inhibition was shown to activate NF-κB signaling in different cellular systems,[27,30,31] which we confirmed in our distinct TRAF2-dependent mouse models. At present, it is unclear if canonical or noncanonical NF-κB functions or even both of them were responsible for the LPC$^{\Delta Traf2,\ Casp8}$ phenotype and the conversion from sublethal to lethal necrosome activation in hepatocytes. This question could not be addressed with the models we used in this study because any intervention involving IKKβ, NEMO, or RelA would affect p52-dependent pathways.[32] To further address this question, additional subcrossing strategies deleting e.g. *Ikka*, *Nik*, or *Nfkb2* would be required.

Sublethal necrosome activation was associated with an accumulation of two distinct MoMF subsets characterized by profibrotic and procarcinogenic gene-expression patterns. These macrophage populations presumably enhanced the proinflammatory microenvironment and thus augmented tumorigenesis. Our experiments suggested that CCL20 originated primarily from hepatocytes with sublethal necrosome activation. However, given the long list of upregulated cytokines and chemokines in LPC$^{\Delta Traf2,\ Casp8}$ livers, it is likely that next to CCL20, other NF-κB-dependent cytokines and chemokines released from LPC$^{\Delta Traf2,\ Casp8}$ hepatocytes contributed to inflammation and hepatocarcinogenesis. LPC$^{\Delta Traf2,\ Casp8}$-*Ripk3*$^{-/-}$ and LPC$^{\Delta Traf2,\ Casp8,\ Ikbkb}$ livers showed comparable immune signatures, which were also similar to those of WT mice. This finding suggested that neither pure NF-κB activation without cell-death execution (LPC$^{\Delta Traf2,\ Casp8}$-*Ripk3*$^{-/-}$ mice) nor necroptosis without NF-κB activation (LPC$^{\Delta Traf2,\ Casp8,\ Ikbkb}$ mice) triggered an enhanced immune response and thus failed to induce liver cancer.

It is a general dogma that malignant transformation occurs as a consequence of the accumulation of genomic aberrations, leading to cancer development.[55] Our analysis showed that cell death played an important role in the initiation of genetic aberrations. However, despite the similar initial genetic situation, tumors only manifested in livers in which NF-κB was activated. Conversely, our data showed that inflammation alone without chronic cell death was not sufficient to induce tumors, which is an important finding in the light of previous data on NF-κB hyperactivation and hepatocarcinogenesis.[56,57]

While apoptosis is activated in distinct human liver diseases such as viral hepatitis,[58] we and others provided evidence that necroptosis is relevant in human NASH and nonalcoholic fatty-liver disease (NAFLD),[5,59] representing major disease entities driving the risk for the development of HCC in the Western world.[60] Similarly, necroptosis has been shown to promote alcoholic liver disease.[61] Therefore, our data could provide an important basis for the development of a chemoprevention strategies against HCC in metabolic liver disease in high-risk patients. Long-term systemic pharmacological inhibition of cell-death pathways might be associated with unwanted side effects like lymphoma development as observed spontaneously in *Casp8*$^{-/-}$*Ripk3*$^{-/-}$ mice.[62,63] Furthermore, alternative cell-death pathways might also be inadvertently activated, as seen in obese RIPK3-deficient mice, in which glucose intolerance occurred due to increased adipocyte apoptosis.[59] Therefore, our present findings implicate that instead of targeting necroptosis, pharmacological targeting of necroptosis-response pathways might be a safe and effective strategy to disarm the carcinogenic potential of necroptosis signaling.

Limitations of the study

The approach of *in vivo* two-photon microscopy, in which we identified the sublethal necroptosis signaling mechanism in mice, cannot be transferred directly to the situation in humans. Although we identified a small number of human hepatocytes with leaky membranes and active membrane potential *in vitro*,

(B) Leakiness of PI-positive hepatocytes of an LPC$^{\Delta Traf2,\ Casp8}$ mouse in relation to dextran (3,000 Da). Dextran-associated fluorescence intensity is shown in a blood sinusoid, a PI-positive, 'leaky' hepatocyte and a PI-negative, "normal" hepatocyte. Tail vein bolus injections of dextran were given at min 0 and 60 of the imaging period. The corresponding video is Video S5.

(C) Correlation of dextran- and PI-associated fluorescence intensity in the LPC$^{\Delta Traf2,\ Casp8}$ mice. Nuclear (PI) and cytoplasmic (dextran) fluorescence were analyzed in 268 hepatocytes from 3 mice.

(D–F) Stills from intravital videos of an LPC$^{\Delta Traf2,\ Casp8}$ and an LPC$^{\Delta Traf2,\ Casp8,\ Ikbkb}$ mouse. Scale bars: 50 μm. The cells indicated by red circles where quantitatively analyzed in LPC$^{\Delta Traf2,\ Casp8}$ (E) and LPC$^{\Delta Traf2,\ Casp8,\ Ikbkb}$ (F) mice.

(G) Kaplan-Meier analysis of the time until loss of mitochondrial potential of PI-positive or SYTOX green-positive hepatocytes. Totally, 152 PI-positive hepatocytes from 20 LPC$^{\Delta Traf2,\ Casp8}$ and 20 PI-positive hepatocytes from 8 LPC$^{\Delta Traf2,\ Casp8,\ Ikbkb}$ mice were analyzed. The p value of the log-rank test is given.

See also Figures S4 and S5 and Videos S1–S6.

implicating sublethal necroptosis signaling, it is currently unclear whether sublethal necroptosis signaling also occurs in human disease. Further improvement of noninvasive imaging techniques such as magnetic resonance imaging (MRI) could help to address this question in the future.

STAR★METHODS

Detailed methods are provided in the online version of this paper and include the following:

- KEY RESOURCES TABLE
- RESOURCE AVAILABILITY
  - Lead contact
  - Materials availability
  - Data and code availability
- EXPERIMENTAL MODEL AND SUBJECT DETAILS
  - Generation of conditional genetically ablated mice
  - Human Liver Samples
- METHOD DETAILS
  - Liver Injury Models
  - Clodronate-Liposome Model
  - Anti TNF Treatment with Etanercept
  - Primary Hepatocyte Culturing
  - Magnetic-Activated Cell Sorting (MACS) using anti-CD45 Microbeads
  - *Traf2*$^{-/-}$ MEF Culture
  - *In Vitro* Live Cell Imaging
  - Serum-Analysis
  - Western blot Analysis
  - Electrophoretic Mobility Shift Assay (EMSA)
  - Quantitative Real-Time PCR
  - Stainings
  - TUNEL
  - *In situ* hybridisation by RNAScope® Chromogenic
  - Transmission Electron Microscopy
  - 3D Reconstruction of the Biliary System
  - Array Comparative Genomic Hybridization (aCGH) Analysis
  - Micro-Array
  - RNA Sequencing
  - Single Cell RNA Processing, Clustering and Annotation
  - Measurement of Cytokines
  - Determination of CCL20 Concentrations by ELISA
  - Intravital Imaging
  - Image Analysis and Statistical Evaluation
- QUANTIFICATION AND STATISTICAL ANALYSIS
  - Statistics
  - Analysis and Quantification of Immunohistochemical Stainings and TUNEL

ACKNOWLEDGMENTS

The authors would like to express their gratitude to the following scientists for kindly providing mouse models: R. Brink and the Centenary (Sydney, Australia): *Traf2*$^{Fl/Fl}$ mice, W. Alexander and the WEHI (Melbourne, Australia): *Mlkl*$^{Fl/Fl}$ mice, C. Trautwein/C. Liedtke (Aachen, Germany): *Nemo*$^{Fl/Fl}$ mice, V. Dixit (San Francisco, USA): *Ripk3*$^{-/-}$ mice, S. Akira (Osaka, Japan): *Tak1*$^{Fl/Fl}$ mice, M. Karin (San Diego, USA): *Ikk*β$^{Fl/Fl}$ mice, R. Hakem (Toronto, Canada): *Casp-8*$^{Fl/Fl}$. The authors would like to thank H. Königs-Werner and the Electron Microscopic Facility at the University Hospital RWTH Aachen, Germany for their excellent support. The authors are grateful for technical support from D. Heide, N. Eichhorst, M. Suzanj, T. Janssen, M. Fastrich, V. Herbertz, C. Ruprecht, K. Wehr, R. Hillermann, O. Seelbach, J. Gautheron, and F. Reisinger. T. Luedde was funded by the European Research Council (ERC) under the European Union's Horizon 2020 research and innovation program through the ERC Consolidator Grant "PhaseControl" (grant agreement 771083). T. Luedde was further funded by the German Cancer Aid (Deutsche Krebshilfe 70114893), the German Research Foundation (DFG – LU 1360/3-2 (279874820), LU 1360/4-(1461704932), CA830/3-1 and SFB-CRC 1382 Project A01) and the German Ministry of Health (BMG—DEEP LIVER 2520DAT111). M.V. was supported by the German Cancer Aid (Deutsche Krebshilfe —70114893) and the research committee of the Medical Faculty of the Heinrich Heine University. A.S. was supported by the German Research Foundation (DFG – SCHN 1659/1-1). T. Luedde, M.V., and A.S. received funding from the Ministry of Culture and Science of the State of North Rhine-Westphalia (CANTAR—NW21-062E). M.C. was supported by the German Research Foundation (DFG) CA830/3-1. M.H. was supported by the German Research Foundation (SFBTR-179 project ID 272983813, SFBTR-209 project ID 314905040, SFB-1479 project ID: 441891347-P10 and SFB-TR209) and an ERC Consolidator grant (LiverHepatoMetabopath) under grant agreement no 667273. A.G., J.G.H., and JG.B. were funded by the Federal Ministry of Education and Research (BMBF, Germany) Liver-LiSyM grant FKZ 031L0052 (to A.G.), FKZ 031L0045 and 031L0257D (to J.G.H), and C-TIP-HCC 031L0257G (to J.G.B.). A.G. was funded by the German Research Foundation (DFG; GH 276/1-1; Project no. 457840828). CRUK program grants, references C18342/A23390 and C9380/A18084 supported D.A.M. and F.O. A.L.S. was supported by National Health and Medical Research Council of Australia (NHMRC; grant 2002965) and J.M.M. by NHMRC grants 1172929 and 9000719. M.S.J. was supported by a Mildred Scheel Postdoc fellowship (57584079). A.L.L and A.W. were funded by the Swiss National Science Foundation (SNF 320030-182764).

AUTHOR CONTRIBUTIONS

M.V. and T. Luedde designed and guided the research. T. Luedde and M.V. wrote the manuscript with help from other authors. M.V. performed and analyzed most of the experiments. A.T.S., A.A., M.Ca., M.T.S., V.B., L.S.K., L.K., M.K., B.G., C.K., K.U., A.L.L., W.A., M.T.K., S.H.L., C.L., M.S.J., O.G., M.V.B., S.J., S.G., J.E.B.A., C.V.M., V.M., J.M.L., R.W., J.N.K., M.L., L.R.H., A.B., D.S., A.L.C., G.N., F.O., B.L., G.F., C.R., and T.A. contributed to research design and/or conducted experiments. A.G and J.G.H. designed, performed, and analyzed the intravital imaging experiments and contributed to research design. M.Ch., S.H., and I.G.C. analyzed the single-cell RNA-seq. P.S., M.T., F.T., T. Lammers, D.A.M., J.G.B., V.K., U.P.N., R.S.K., R.K., F.G., A.V., A.L.S., J.M.M., J.G.H., and M.H. provided important technical support and intellectual input. A.W. and T. Longerich conducted histopathological analyses.

DECLARATION OF INTERESTS

A.L.S. and J.M.M. contribute to a project developing necroptosis inhibitors in collaboration with Anaxis Pharma.

INCLUSION AND DIVERSITY

We support inclusive, diverse, and equitable conduct of research.

Received: January 14, 2022
Revised: August 30, 2022
Accepted: May 22, 2023
Published: June 16, 2023

REFERENCES

1. Rizvi, S., Wang, J., and El-Khoueiry, A.B. (2021). Liver cancer immunity. Hepatology *73*, 86–103. https://doi.org/10.1002/hep.31416.
2. Leone, V., Ali, A., Weber, A., Tschaharganeh, D.F., and Heikenwalder, M. (2021). Liver inflammation and hepatobiliary cancers. Trends Cancer *7*, 606–623. https://doi.org/10.1016/j.trecan.2021.01.012.

3. Aizawa, S., Brar, G., and Tsukamoto, H. (2020). Cell death and liver disease. Gut Liver *14*, 20–29. https://doi.org/10.5009/gnl18486.

4. Dai, W., Cheng, J., Leng, X., Hu, X., and Ao, Y. (2021). The potential role of necroptosis in clinical diseases (review). Int. J. Mol. Med. *47*, 89. https://doi.org/10.3892/ijmm.2021.4922.

5. Gautheron, J., Vucur, M., Reisinger, F., Cardenas, D.V., Roderburg, C., Koppe, C., Kreggenwinkel, K., Schneider, A.T., Bartneck, M., Neumann, U.P., et al. (2014). A positive feedback loop between RIP3 and JNK controls non-alcoholic steatohepatitis. EMBO Mol. Med. *6*, 1062–1074. https://doi.org/10.15252/emmm.201403856.

6. Llovet, J.M., Kelley, R.K., Villanueva, A., Singal, A.G., Pikarsky, E., Roayaie, S., Lencioni, R., Koike, K., Zucman-Rossi, J., and Finn, R.S. (2021). Hepatocellular carcinoma. Nat. Rev. Dis. Primers *7*, 6. https://doi.org/10.1038/s41572-020-00240-3.

7. Dondelinger, Y., Jouan-Lanhouet, S., Divert, T., Theatre, E., Bertin, J., Gough, P.J., Giansanti, P., Heck, A.J., Dejardin, E., Vandenabeele, P., and Bertrand, M.J. (2015). NF-κB-independent role of IKKα/IKKβ in preventing RIPK1 kinase-dependent apoptotic and necroptotic cell death during TNF signaling. Mol. Cell *60*, 63–76. https://doi.org/10.1016/j.molcel.2015.07.032.

8. Tang, D., Kang, R., Berghe, T.V., Vandenabeele, P., and Kroemer, G. (2019). The molecular machinery of regulated cell death. Cell Res. *29*, 347–364. https://doi.org/10.1038/s41422-019-0164-5.

9. Nakano, H., Murai, S., and Moriwaki, K. (2022). Regulation of the release of damage-associated molecular patterns from necroptotic cells. Biochem. J. *479*, 677–685. https://doi.org/10.1042/BCJ20210604.

10. Kearney, C.J., and Martin, S.J. (2017). An inflammatory perspective on necroptosis. Mol. Cell *65*, 965–973. https://doi.org/10.1016/j.molcel.2017.02.024.

11. Gong, Y.N., Crawford, J.C., Heckmann, B.L., and Green, D.R. (2019). To the edge of cell death and back. FEBS Journal *286*, 430–440. https://doi.org/10.1111/febs.14714.

12. Wang, W., Prokopec, J.S., Zhang, Y., Sukhoplyasova, M., Shinglot, H., Wang, M.T., Linkermann, A., Stewart-Ornstein, J., and Gong, Y.N. (2022). Sensing plasma membrane pore formation induces chemokine production in survivors of regulated necrosis. Dev. Cell *57*, 228–245.e6. https://doi.org/10.1016/j.devcel.2021.12.015.

13. Mifflin, L., Ofengeim, D., and Yuan, J. (2020). Receptor-interacting protein kinase 1 (RIPK1) as a therapeutic target. Nat. Rev. Drug Discov. *19*, 553–571. https://doi.org/10.1038/s41573-020-0071-y.

14. Samson, A.L., Fitzgibbon, C., Patel, K.M., Hildebrand, J.M., Whitehead, L.W., Rimes, J.S., Jacobsen, A.V., Horne, C.R., Gavin, X.J., Young, S.N., et al. (2021). A toolbox for imaging RIPK1, RIPK3, and MLKL in mouse and human cells. Cell Death Differ. *28*, 2126–2144. https://doi.org/10.1038/s41418-021-00742-x.

15. Horne, C.R., Samson, A.L., and Murphy, J.M. (2023). The web of death: the expanding complexity of necroptotic signaling. Trends Cell Biol. *33*, 162–174. https://doi.org/10.1016/j.tcb.2022.05.008.

16. Vucur, M., Reisinger, F., Gautheron, J., Janssen, J., Roderburg, C., Cardenas, D.V., Kreggenwinkel, K., Koppe, C., Hammerich, L., Hakem, R., et al. (2013). RIP3 inhibits inflammatory hepatocarcinogenesis but promotes cholestasis by controlling caspase-8- and JNK-dependent compensatory cell proliferation. Cell Rep. *4*, 776–790. https://doi.org/10.1016/j.celrep.2013.07.035.

17. Müller, T., Dewitz, C., Schmitz, J., Schröder, A.S., Bräsen, J.H., Stockwell, B.R., Murphy, J.M., Kunzendorf, U., and Krautwald, S. (2017). Necroptosis and ferroptosis are alternative cell death pathways that operate in acute kidney failure. Cell. Mol. Life Sci. *74*, 3631–3645. https://doi.org/10.1007/s00018-017-2547-4.

18. Yin, Q., Lamothe, B., Darnay, B.G., and Wu, H. (2009). Structural basis for the lack of E2 interaction in the RING domain of TRAF2. Biochemistry *48*, 10558–10567. https://doi.org/10.1021/bi901462e.

19. Vucic, D. (2011). TRAF2 and cellular IAPs: a critical link in TNFR family signaling. Adv. Exp. Med. Biol. *691*, 63–78. https://doi.org/10.1007/978-1-4419-6612-4_7.

20. Petersen, S.L., Chen, T.T., Lawrence, D.A., Marsters, S.A., Gonzalvez, F., and Ashkenazi, A. (2015). TRAF2 is a biologically important necroptosis suppressor. Cell Death Differ. *22*, 1846–1857. https://doi.org/10.1038/cdd.2015.35.

21. Schneider, A.T., Gautheron, J., Feoktistova, M., Roderburg, C., Loosen, S.H., Roy, S., Benz, F., Schemmer, P., Büchler, M.W., Nachbur, U., et al. (2017). RIPK1 suppresses a TRAF2-dependent pathway to liver cancer. Cancer Cell *31*, 94–109. https://doi.org/10.1016/j.ccell.2016.11.009.

22. Krishna-Subramanian, S., Singer, S., Armaka, M., Banales, J.M., Holzer, K., Schirmacher, P., Walczak, H., Kollias, G., Pasparakis, M., and Kondylis, V. (2019). RIPK1 and death receptor signaling drive biliary damage and early liver tumorigenesis in mice with chronic hepatobiliary injury. Cell Death Differ. *26*, 2710–2726. https://doi.org/10.1038/s41418-019-0330-9.

23. Terracciano, L., and Tornillo, L. (2003). Cytogenetic alterations in liver cell tumors as detected by comparative genomic hybridization. Pathologica *95*, 71–82.

24. Bettermann, K., Vucur, M., Haybaeck, J., Koppe, C., Janssen, J., Heymann, F., Weber, A., Weiskirchen, R., Liedtke, C., Gassler, N., et al. (2010). TAK1 suppresses a NEMO-dependent but NF-kappaB-independent pathway to liver cancer. Cancer Cell *17*, 481–496. https://doi.org/10.1016/j.ccr.2010.03.021.

25. Takaesu, G., Surabhi, R.M., Park, K.J., Ninomiya-Tsuji, J., Matsumoto, K., and Gaynor, R.B. (2003). TAK1 is critical for IkappaB kinase-mediated activation of the NF-kappaB pathway. J. Mol. Biol. *326*, 105–115. https://doi.org/10.1016/s0022-2836(02)01404-3.

26. Inokuchi, S., Aoyama, T., Miura, K., Osterreicher, C.H., Kodama, Y., Miyai, K., Akira, S., Brenner, D.A., and Seki, E. (2010). Disruption of TAK1 in hepatocytes causes hepatic injury, inflammation, fibrosis, and carcinogenesis. Proc. Natl. Acad. Sci. USA *107*, 844–849. https://doi.org/10.1073/pnas.0909781107.

27. Tada, K., Okazaki, T., Sakon, S., Kobarai, T., Kurosawa, K., Yamaoka, S., Hashimoto, H., Mak, T.W., Yagita, H., Okumura, K., et al. (2001). Critical roles of TRAF2 and TRAF5 in tumor necrosis factor-induced NF-kappa B activation and protection from cell death. J. Biol. Chem. *276*, 36530–36534. https://doi.org/10.1074/jbc.M104837200.

28. Koppe, C., Verheugd, P., Gautheron, J., Reisinger, F., Kreggenwinkel, K., Roderburg, C., Quagliata, L., Terracciano, L., Gassler, N., Tolba, R.H., et al. (2016). IκB kinaseα/β control biliary homeostasis and hepatocarcinogenesis in mice by phosphorylating the cell-death mediator receptor-interacting protein kinase 1. Hepatology *64*, 1217–1231. https://doi.org/10.1002/hep.28723.

29. Koppe, C., Reisinger, F., Wehr, K., Vucur, M., Trautwein, C., Tacke, F., Heikenwalder, M., and Luedde, T. (2019). An NF-kappaB- and IKK-independent function of NEMO prevents hepatocarcinogenesis by suppressing compensatory liver regeneration. Cancers *11*. https://doi.org/10.3390/cancers11070999.

30. Varfolomeev, E., Blankenship, J.W., Wayson, S.M., Fedorova, A.V., Kayagaki, N., Garg, P., Zobel, K., Dynek, J.N., Elliott, L.O., Wallweber, H.J., et al. (2007). IAP antagonists induce autoubiquitination of c-IAPs, NF-kappaB activation, and TNFalpha-dependent apoptosis. Cell *131*, 669–681. https://doi.org/10.1016/j.cell.2007.10.030.

31. Zhang, J., Webster, J.D., Dugger, D.L., Goncharov, T., Roose-Girma, M., Hung, J., Kwon, Y.C., Vucic, D., Newton, K., and Dixit, V.M. (2019). Ubiquitin ligases cIAP1 and cIAP2 limit cell death to prevent inflammation. Cell Rep. *27*, 2679–2689.e3. https://doi.org/10.1016/j.celrep.2019.04.111.

32. Lombardi, L., Ciana, P., Cappellini, C., Trecca, D., Guerrini, L., Migliazza, A., Maiolo, A.T., and Neri, A. (1995). Structural and functional characterization of the promoter regions of the NFkB2 gene. Nucleic Acids Res. *23*, 2328–2336. https://doi.org/10.1093/nar/23.12.2328.

33. Hass, H.G., Jobst, J., Scheurlen, M., Vogel, U., and Nehls, O. (2015). Gene expression analysis for evaluation of potential biomarkers in hepatocellular carcinoma. Anticancer Res. *35*, 2021–2028.

34. Tovar, V., Alsinet, C., Villanueva, A., Hoshida, Y., Chiang, D.Y., Solé, M., Thung, S., Moyano, S., Toffanin, S., Mínguez, B., et al. (2010). IGF activation in a molecular subclass of hepatocellular carcinoma and pre-clinical efficacy of IGF-1R blockage. J. Hepatol. *52*, 550–559. https://doi.org/10.1016/j.jhep.2010.01.015.

35. Chiang, D.Y., Villanueva, A., Hoshida, Y., Peix, J., Newell, P., Minguez, B., LeBlanc, A.C., Donovan, D.J., Thung, S.N., Solé, M., et al. (2008). Focal gains of VEGFA and molecular classification of hepatocellular carcinoma. Cancer Res. *68*, 6779–6788. https://doi.org/10.1158/0008-5472.CAN-08-0742.

36. Hoshida, Y., Nijman, S.M., Kobayashi, M., Chan, J.A., Brunet, J.P., Chiang, D.Y., Villanueva, A., Newell, P., Ikeda, K., Hashimoto, M., et al. (2009). Integrative transcriptome analysis reveals common molecular subclasses of human hepatocellular carcinoma. Cancer Res. *69*, 7385–7392. https://doi.org/10.1158/0008-5472.CAN-09-1089.

37. Coulouarn, C., Factor, V.M., and Thorgeirsson, S.S. (2008). Transforming growth factor-beta gene expression signature in mouse hepatocytes predicts clinical outcome in human cancer. Hepatology *47*, 2059–2067. https://doi.org/10.1002/hep.22283.

38. Villanueva, A., Hoshida, Y., Battiston, C., Tovar, V., Sia, D., Alsinet, C., Cornella, H., Liberzon, A., Kobayashi, M., Kumada, H., et al. (2011). Combining clinical, pathology, and gene expression data to predict recurrence of hepatocellular carcinoma. Gastroenterology *140*. 1501-12.e2. https://doi.org/10.1053/j.gastro.2011.02.006.

39. Andersen, J.B., Loi, R., Perra, A., Factor, V.M., Ledda-Columbano, G.M., Columbano, A., and Thorgeirsson, S.S. (2010). Progenitor-derived hepatocellular carcinoma model in the rat. Hepatology *51*, 1401–1409. https://doi.org/10.1002/hep.23488.

40. Villanueva, A., Alsinet, C., Yanger, K., Hoshida, Y., Zong, Y., Toffanin, S., Rodriguez-Carunchio, L., Solé, M., Thung, S., Stanger, B.Z., et al. (2012). Notch signaling is activated in human hepatocellular carcinoma and induces tumor formation in mice. Gastroenterology *143*, 1660–1669.e7. https://doi.org/10.1053/j.gastro.2012.09.002.

41. Mínguez, B., Hoshida, Y., Villanueva, A., Toffanin, S., Cabellos, L., Thung, S., Mandeli, J., Sia, D., April, C., Fan, J.B., et al. (2011). Gene-expression signature of vascular invasion in hepatocellular carcinoma. J. Hepatol. *55*, 1325–1331. https://doi.org/10.1016/j.jhep.2011.02.034.

42. Villanueva, A., Portela, A., Sayols, S., Battiston, C., Hoshida, Y., Méndez-González, J., Imbeaud, S., Letouzé, E., Hernandez-Gea, V., Cornella, H., et al. (2015). DNA methylation-based prognosis and epidrivers in hepatocellular carcinoma. Hepatology *61*, 1945–1956. https://doi.org/10.1002/hep.27732.

43. Chen, W., Qin, Y., and Liu, S. (2020). CCL20 signaling in the tumor microenvironment. Adv. Exp. Med. Biol. *1231*, 53–65. https://doi.org/10.1007/978-3-030-36667-4_6.

44. Aran, D., Looney, A.P., Liu, L., Wu, E., Fong, V., Hsu, A., Chak, S., Naikawadi, R.P., Wolters, P.J., Abate, A.R., et al. (2019). Reference-based analysis of lung single-cell sequencing reveals a transitional profibrotic macrophage. Nat. Immunol. *20*, 163–172. https://doi.org/10.1038/s41590-018-0276-y.

45. Hashimoto, O., Yoshida, M., Koma, Y., Yanai, T., Hasegawa, D., Kosaka, Y., Nishimura, N., and Yokozaki, H. (2016). Collaboration of cancer-associated fibroblasts and tumour-associated macrophages for neuroblastoma development. J. Pathol. *240*, 211–223. https://doi.org/10.1002/path.4769.

46. Roumenina, L.T., Daugan, M.V., Noé, R., Petitprez, F., Vano, Y.A., Sanchez-Salas, R., Becht, E., Meilleroux, J., Clec'h, B.L., Giraldo, N.A., et al. (2019). Tumor cells hijack macrophage-produced complement C1q to promote tumor growth. Cancer Immunol Res *7*, 1091–1105. https://doi.org/10.1158/2326-6066.Cir-18-0891.

47. Zhu, F., Li, X., Chen, S., Zeng, Q., Zhao, Y., and Luo, F. (2016). Tumor-associated macrophage or chemokine ligand CCL17 positively regulates the tumorigenesis of hepatocellular carcinoma. Med. Oncol. *33*, 17. https://doi.org/10.1007/s12032-016-0729-9.

48. Kroemer, G., Galluzzi, L., and Brenner, C. (2007). Mitochondrial membrane permeabilization in cell death. Physiol. Rev. *87*, 99–163. https://doi.org/10.1152/physrev.00013.2006.

49. Ghallab, A., Hofmann, U., Sezgin, S., Vartak, N., Hassan, R., Zaza, A., Godoy, P., Schneider, K.M., Guenther, G., Ahmed, Y.A., et al. (2019). Bile microinfarcts in cholestasis are initiated by rupture of the apical hepatocyte membrane and cause shunting of bile to sinusoidal blood. Hepatology *69*, 666–683. https://doi.org/10.1002/hep.30213.

50. Pérez-Garijo, A. (2018). When dying is not the end: apoptotic caspases as drivers of proliferation. Semin. Cell Dev. Biol. *82*, 86–95. https://doi.org/10.1016/j.semcdb.2017.11.036.

51. Dara, L. (2018). The receptor interacting protein kinases in the liver. Semin. Liver Dis. *38*, 73–86. https://doi.org/10.1055/s-0038-1629924.

52. Preston, S.P., Stutz, M.D., Allison, C.C., Nachbur, U., Gouil, Q., Tran, B.M., Duvivier, V., Arandjelovic, P., Cooney, J.P., Mackiewicz, L., et al. (2022). Epigenetic silencing of RIPK3 in hepatocytes prevents MLKL-mediated necroptosis from contributing to liver pathologies. Gastroenterology *163*, 1643–1657.e14. https://doi.org/10.1053/j.gastro.2022.08.040.

53. Zhao, Q., Guo, J., Cheng, X., Liao, Y., Bi, Y., Gong, Y., Zhang, X., Guo, Y., Wang, X., Yu, W., et al. (2021). RIPK3 suppresses the progression of spontaneous intestinal tumorigenesis. Front. Oncol. *11*, 664927. https://doi.org/10.3389/fonc.2021.664927.

54. Geserick, P., Wang, J., Schilling, R., Horn, S., Harris, P.A., Bertin, J., Gough, P.J., Feoktistova, M., and Leverkus, M. (2015). Absence of RIPK3 predicts necroptosis resistance in malignant melanoma. Cell Death Dis. *6*, e1884. https://doi.org/10.1038/cddis.2015.240.

55. Woodman, S.E., and Mills, G.B. (2010). Are oncogenes sufficient to cause human cancer? Proc. Natl. Acad. Sci. USA *107*, 20599–20600. https://doi.org/10.1073/pnas.1015563107.

56. Giuliani, C., Bucci, I., and Napolitano, G. (2018). The role of the transcription factor nuclear factor-kappa B in thyroid autoimmunity and cancer. Front. Endocrinol. (Lausanne) *9*, 471. https://doi.org/10.3389/fendo.2018.00471.

57. Finkin, S., Yuan, D., Stein, I., Taniguchi, K., Weber, A., Unger, K., Browning, J.L., Goossens, N., Nakagawa, S., Gunasekaran, G., et al. (2015). Ectopic lymphoid structures function as microniches for tumor progenitor cells in hepatocellular carcinoma. Nat. Immunol. *16*, 1235–1244. https://doi.org/10.1038/ni.3290.

58. Luedde, T., Kaplowitz, N., and Schwabe, R.F. (2014). Cell death and cell death responses in liver disease: mechanisms and clinical relevance. Gastroenterology *147*, 765–783.e4. https://doi.org/10.1053/j.gastro.2014.07.018.

59. Gautheron, J., Vucur, M., Schneider, A.T., Severi, I., Roderburg, C., Roy, S., Bartneck, M., Schrammen, P., Diaz, M.B., Ehling, J., et al. (2016). The necroptosis-inducing kinase RIPK3 dampens adipose tissue inflammation and glucose intolerance. Nat. Commun. *7*, 11869. https://doi.org/10.1038/ncomms11869.

60. Anstee, Q.M., Reeves, H.L., Kotsiliti, E., Govaere, O., and Heikenwalder, M. (2019). From NASH to HCC: current concepts and future challenges. Nat. Rev. Gastroenterol. Hepatol. *16*, 411–428. https://doi.org/10.1038/s41575-019-0145-7.

61. Newton, K. (2015). RIPK1 and RIPK3: critical regulators of inflammation and cell death. Trends Cell Biol. *25*, 347–353. https://doi.org/10.1016/j.tcb.2015.01.001.

62. Oberst, A., Dillon, C.P., Weinlich, R., McCormick, L.L., Fitzgerald, P., Pop, C., Hakem, R., Salvesen, G.S., and Green, D.R. (2011). Catalytic activity of the caspase-8-FLIP(L) complex inhibits RIPK3-dependent necrosis. Nature *471*, 363–367. https://doi.org/10.1038/nature09852.

63. Kaiser, W.J., Upton, J.W., Long, A.B., Livingston-Rosanoff, D., Daley-Bauer, L.P., Hakem, R., Caspary, T., and Mocarski, E.S. (2011). RIP3 mediates the embryonic lethality of caspase-8-deficient mice. Nature *471*, 368–372. https://doi.org/10.1038/nature09857.

64. Love, M.I., Huber, W., and Anders, S. (2014). Moderated estimation of fold change and dispersion for RNA-seq data with DESeq2. Genome Biol. *15*, 550. https://doi.org/10.1186/s13059-014-0550-8.

65. Grech, A.P., Amesbury, M., Chan, T., Gardam, S., Basten, A., and Brink, R. (2004). TRAF2 differentially regulates the canonical and noncanonical pathways of NF-kappaB activation in mature B cells. Immunity *21*, 629–642. https://doi.org/10.1016/j.immuni.2004.09.011.

66. Kellendonk, C., Opherk, C., Anlag, K., Schütz, G., and Tronche, F. (2000). Hepatocyte-specific expression of Cre recombinase. Genesis *26*, 151–153. https://doi.org/10.1002/(sici)1526-968x(200002)26:2<151::aid-gene17>3.0.co;2-e.

67. Salmena, L., Lemmers, B., Hakem, A., Matysiak-Zablocki, E., Murakami, K., Au, P.Y., Berry, D.M., Tamblyn, L., Shehabeldin, A., Migon, E., et al. (2003). Essential role for caspase 8 in T-cell homeostasis and T-cell-mediated immunity. Genes Dev. *17*, 883–895. https://doi.org/10.1101/gad.1063703.

68. Murphy, J.M., Czabotar, P.E., Hildebrand, J.M., Lucet, I.S., Zhang, J.G., Alvarez-Diaz, S., Lewis, R., Lalaoui, N., Metcalf, D., Webb, A.I., et al. (2013). The pseudokinase MLKL mediates necroptosis via a molecular switch mechanism. Immunity *39*, 443–453. https://doi.org/10.1016/j.immuni.2013.06.018.

69. Beraza, N., Malato, Y., Sander, L.E., Al-Masaoudi, M., Freimuth, J., Riethmacher, D., Gores, G.J., Roskams, T., Liedtke, C., and Trautwein, C. (2009). Hepatocyte-specific NEMO deletion promotes NK/NKT cell- and TRAIL-dependent liver damage. J. Exp. Med. *206*, 1727–1737. https://doi.org/10.1084/jem.20082152.

70. Greten, F.R., Arkan, M.C., Bollrath, J., Hsu, L.C., Goode, J., Miething, C., Göktuna, S.I., Neuenhahn, M., Fierer, J., Paxian, S., et al. (2007). NF-kappaB is a negative regulator of IL-1beta secretion as revealed by genetic and pharmacological inhibition of IKKbeta. Cell *130*, 918–931. https://doi.org/10.1016/j.cell.2007.07.009.

71. Müller, K., Honcharova-Biletska, H., Koppe, C., Egger, M., Chan, L.K., Schneider, A.T., Küsgens, L., Böhm, F., Boege, Y., Healy, M.E., et al. (2021). JNK signaling prevents biliary cyst formation through a caspase-8-dependent function of RIPK1 during aging. Proc. Natl. Acad. Sci. USA *118*. https://doi.org/10.1073/pnas.2007194118.

72. Geisler, F., Algül, H., Paxian, S., and Schmid, R.M. (2007). Genetic inactivation of RelA/p65 sensitizes adult mouse hepatocytes to TNF-induced apoptosis in vivo and in vitro. Gastroenterology *132*, 2489–2503. https://doi.org/10.1053/j.gastro.2007.03.033.

73. Newton, K., Sun, X., and Dixit, V.M. (2004). Kinase RIP3 is dispensable for normal NF-kappa Bs, signaling by the B-cell and T-cell receptors, tumor necrosis factor receptor 1, and toll-like receptors 2 and 4. Mol. Cell. Biol. *24*, 1464–1469. https://doi.org/10.1128/MCB.24.4.1464-1469.2004.

74. Albrecht, W., Kappenberg, F., Brecklinghaus, T., Stoeber, R., Marchan, R., Zhang, M., Ebbert, K., Kirschner, H., Grinberg, M., Leist, M., et al. (2019). Prediction of human drug-induced liver injury (DILI) in relation to oral doses and blood concentrations. Arch. Toxicol. *93*, 1609–1637. https://doi.org/10.1007/s00204-019-02492-9.

75. Luedde, T., Heinrichsdorff, J., de Lorenzi, R., De Vos, R., Roskams, T., and Pasparakis, M. (2008). IKK1 and IKK2 cooperate to maintain bile duct integrity in the liver. Proc. Natl. Acad. Sci. USA *105*, 9733–9738. https://doi.org/10.1073/pnas.0800198105.

76. Lin, K., Kools, H., de Groot, P.J., Gavai, A.K., Basnet, R.K., Cheng, F., Wu, J., Wang, X., Lommen, A., Hooiveld, G.J., et al. (2011). MADMAX - Management and analysis database for multiple ~omics experiments. J. Integr. Bioinform. *8*, 160. https://doi.org/10.2390/biecoll-jib-2011-160.

77. Bolstad, B.M., Irizarry, R.A., Astrand, M., and Speed, T.P. (2003). A comparison of normalization methods for high density oligonucleotide array data based on variance and bias. Bioinformatics *19*, 185–193. https://doi.org/10.1093/bioinformatics/19.2.185.

78. Irizarry, R.A., Bolstad, B.M., Collin, F., Cope, L.M., Hobbs, B., and Speed, T.P. (2003). Summaries of Affymetrix GeneChip probe level data. Nucleic Acids Res. *31*, e15. https://doi.org/10.1093/nar/gng015.

79. Dai, M., Wang, P., Boyd, A.D., Kostov, G., Athey, B., Jones, E.G., Bunney, W.E., Myers, R.M., Speed, T.P., Akil, H., et al. (2005). Evolving gene/transcript definitions significantly alter the interpretation of GeneChip data. Nucleic Acids Res. *33*, e175. https://doi.org/10.1093/nar/gni179.

80. Sartor, M.A., Tomlinson, C.R., Wesselkamper, S.C., Sivaganesan, S., Leikauf, G.D., and Medvedovic, M. (2006). Intensity-based hierarchical Bayes method improves testing for differentially expressed genes in microarray experiments. BMC Bioinformatics *7*, 538. https://doi.org/10.1186/1471-2105-7-538.

81. Anders, S., and Huber, W. (2010). Differential expression analysis for sequence count data. Genome Biol. *11*, R106. https://doi.org/10.1186/gb-2010-11-10-r106.

82. Subramanian, A., Tamayo, P., Mootha, V.K., Mukherjee, S., Ebert, B.L., Gillette, M.A., Paulovich, A., Pomeroy, S.L., Golub, T.R., Lander, E.S., et al. (2005). Gene set enrichment analysis: a knowledge-based approach for interpreting genome-wide expression profiles. Proc. Natl. Acad. Sci. USA *102*, 15545–15550. https://doi.org/10.1073/pnas.0506580102.

83. Hoshida, Y. (2010). Nearest template prediction: a single-sample-based flexible class prediction with confidence assessment. PLoS One *5*, e15543. https://doi.org/10.1371/journal.pone.0015543.

84. Butler, A., Hoffman, P., Smibert, P., Papalexi, E., and Satija, R. (2018). Integrating single-cell transcriptomic data across different conditions, technologies, and species. Nat. Biotechnol. *36*, 411–420. https://doi.org/10.1038/nbt.4096.

85. Gu, Z., Eils, R., and Schlesner, M. (2016). Complex heatmaps reveal patterns and correlations in multidimensional genomic data. Bioinformatics *32*, 2847–2849. https://doi.org/10.1093/bioinformatics/btw313.

86. Reif, R., Ghallab, A., Beattie, L., Günther, G., Kuepfer, L., Kaye, P.M., and Hengstler, J.G. (2017). In vivo imaging of systemic transport and elimination of xenobiotics and endogenous molecules in mice. Arch. Toxicol. *91*, 1335–1352. https://doi.org/10.1007/s00204-016-1906-5.

87. Bankhead, P., Loughrey, M.B., Fernández, J.A., Dombrowski, Y., McArt, D.G., Dunne, P.D., McQuaid, S., Gray, R.T., Murray, L.J., Coleman, H.G., et al. (2017). QuPath: open source software for digital pathology image analysis. Sci. Rep. *7*, 16878. https://doi.org/10.1038/s41598-017-17204-5.

88. Schindelin, J., Arganda-Carreras, I., Frise, E., Kaynig, V., Longair, M., Pietzsch, T., Preibisch, S., Rueden, C., Saalfeld, S., Schmid, B., et al. (2012). Fiji - an Open Source platform for biological image analysis. Nat. Methods *9*. https://doi.org/10.1038/nmeth.2019.

STAR★METHODS

KEY RESOURCES TABLE

REAGENT or RESOURCE	SOURCE	IDENTIFIER
Antibodies		
p-MLKL	Abcam	Cat# ab196436; RRID: AB_2687465
MLKL	Biorbyt	Cat# orb32399; RRID: AB_10927389
β−actin	Sigma	Cat# A2066; RRID: AB_476693
Cyclin D1	Thermo	Cat# 333500; RRID: AB_2533114
TRAF2	Santa Cruz	Cat# sc-876; RRID: AB_632533
A20	Cell Signaling	Cat# 5630; RRID: AB_10698880
cleaved Caspase-3	Cell Signaling	Cat# 9661; RRID: AB_2341188
cleaved Caspase-8	Cell Signaling	Cat# 8592; RRID: AB_10891784
pIKKα/β	Cell Signaling	Cat# 2697; RRID: AB_2079382
NF-κB2 p100/p52	Cell signaling	Cat# 4882; RRID: AB_10695537
RIPK3	Cell signaling	Cat# 95702; RRID: AB_2721823
F4/80	Cell signaling	Cat# 70076; RRID: AB_2799771
Caspase-8	Cell signaling	Cat# 4927; RRID: AB_2068301
Caspase-8 (staining)	Enzo	Cat# ALX-804-447-C100; RRID: AB_2050952
IKKβ	Cell signaling	Cat# 8943; RRID: AB_11024092
NEMO	Cell signaling	Cat# 2685; RRID: AB_2124829
RIPK1	BD Biosciences	Cat# 610459; RRID: AB_397832
PCNA	Zymed	Cat# 133900; RRID: AB_86593
GAPDH	ABD Serotec	Cat# MCA 4739; RRID: AB_1720065
rabbit-HRP	Sigma	Cat# GENA934; RRID: AB_2722659
mouse-HRP	Sigma	Cat# GENA931
F4/80	BMA Biochemicals AG	Cat# T-2006; RRID: AB_1227368
B220	BD Pharmingen	Cat# 553084; RRID: AB_394614
CD3	Thermo	Cat# RM-9107-S; RRID: AB_149922
CD206	Proteintech	Cat# 18704-I-AP; RRID: AB_10597232
SOX9	Millipore	Cat# AB5535; RRID: AB_2239761
RIPK3 (staining)	Enzo life science	Cat# ADI-905-242-100; RRID: AB_2039527
pan-Cytokeratin	Dako A/S	Cat# Z0622; RRID: AB_2650434
Collagen IV	Cedarlane	Cat# CL50451AP; RRID: AB_10059811
GP73	Santa Cruz	Cat# sc 48011; RRID: AB_2113325
A6	kindly provided by Dr. Valentina Factor	N/A
Ki67	Thermo	Cat# RM-9106; RRID: AB_2341197
MIP3A/CCL20	Abcam	Cat# ab139585
p50	Santa Cruz	Cat# sc-7178; RRID: AB_650211
p65	Santa Cruz	Cat# sc-372; RRID: AB_632037
α-SMA	Abcam	Cat# ab5694; RRID: AB_2223021
CD45 microbeads	Miltenyi Biotec	Cat# 130-052-301; RRID: AB_2877061
Oligonucleotides		
NF-κB consensus site: 5'-CGGGCT GGGGATTCCCCATCTCGGTAC-3'	MWG	N/A
CCL20: for-ATCAACTCCTGGAGCT GAGAATGG; rev- ATGTACGAGAG GCAACAGTCGTAG	MWG	N/A

(*Continued on next page*)

Continued

REAGENT or RESOURCE	SOURCE	IDENTIFIER
TNF: for-ACCACGCTCTTCTGTCTA CTGA; rev- TCCACTTGGTGGTTTGCTACG	MWG	N/A
IL-6: for-GCTACCAAACTGGATATA ATCAGGA; rev-CCAGGTAGCTATG GTACTCCAGAA	MWG	N/A
LT-α: for-ACCAGTGGCCTCTACTTT GTC; rev-TGGAAGGGGTATTGGGAGGAA	MWG	N/A
LT-β: for-TACACCAGATCCAGGGG TTC; rev-ACTCATCCAAGCGCCTATGA	MWG	N/A
TWEAK: for-CCGCCAGATTGGGGAAT TTAC; rev-AGTCCAAAGTAGGTTAGGAAGGG	MWG	N/A
MCP-1: for-GTGTTGGCTCAGCCAGAT GC; rev- GACACCTGCTGCTGGTGATCC	MWG	N/A
GM-CSF: for-GGCCTTGGAAGCATGTAGA GG; rev-GGAGAACTCGTTAGAGACGACTT	MWG	N/A
S100A6: for-CGCTTCTTCTAGCCCAGT GAT; rev- ACTGGATTTGACCGAGAGAGG	MWG	N/A
A20: for-GAACAGCGATCAGGCCAGG; rev- GGACAGTTGGGTGTCTCACATT	MWG	N/A
Casp-8: for-CGGGGATACTGTCTGATCATCA; rev-CAGAGCCTCTTTATCACAGTCTG	MWG	N/A
TRAF2: for-AGAGAGTAGTTCGGCCTTTCC; rev- GTGCATCCATCATTGGGACAG	MWG	N/A
RIPK3: for- TCT GTC AAG TTA TGG CCT ACT GG; rev- GGA ACA CGA CTC CGA ACC C	MWG	N/A
β-Actin: for-CTCTAGACTTCGAGCAGGAGATGG; rev- ATGCCACAGGATTCCATACCCAAGA	MWG	N/A
Critical Commercial Assays / Items		
CCL20 Elisa	R&D	MCC200
Bio-Plex Pro Mouse Cytokine Grp. I panel	Bio-Rad	N/A
Milliplex Catalog ID.MCYTOMAG-70K-03.Mouse Cytokine MAGNETIC Kit	Merck	MCYTOMAG-70K-03
TUNEL	Promega	G3250
RNeasy Mini Kit	Qiagen	74104
First-Strand Synthesis Kit	Roche	04897030001
Chromium Single Cell 3'Library & Gel Bead Kit v2	10x Genomics	120237
Chromium Single Cell A Chip Kit	10x Genomics	120236
Chromium i7 Multiplex Kit	10x Genomics	120262
RNeasy Microkit columns	Qiagen	74004
Affymetrix WT PLUS reagent kit	Affymetrix	902281
Affymetrix Mouse Gene 1.1 ST array plate	Affymetrix	901420
Glass bottom chambers	Ibidi	80427
RNAScope® 2.5 HD Detection Reagents-RED assay Kit	Advanced Cell Diagnostics (ACD)	322360
Mus musculus-RIPK3 probe		N/A
Human-RIPK3 probe		N/A
Chemicals, peptides, and recombinant proteins		
SYBR Green Reagent	Invitrogen	11760-500
Rhodamine 123	Thermofisher Scientific	R302
Propidium Iodide	Thermofisher Scientific	P1304MP
Dextran, Texas red, 3000 MW	Thermofisher Scientific	D3328

(*Continued on next page*)

Continued

REAGENT or RESOURCE	SOURCE	IDENTIFIER
Hoechst 33258	Thermofisher Scientific	H21491
Hoechst 33342	Thermofisher Scientific	H3570
CD45 Monoclonal Antibody (30-F11), PE	Thermofisher Scientific	12-0451-83
SYTOX Green	Corning, USA	451041
Cholyl-lysyl-fluorescein (CLF)	Thermofisher Scientific	T669
Penicillin-Streptomycin	PAN Biotech	P06-07100
Gentamycin	PAN Biotech	P06-03021
Dulbecco's modified Eagle's Medium (DMEM)	PAN Biotech	P04-03550
Williams E medium	PAN Biotech	P04-29510
Stable glutamine	PAN Biotech	P04-82100
FCS	PAN Biotech	P30-3702
SeraPlus FBS	PAN Biotech	3702-P103009
ITS Supplement	Sigma Aldrich	13146
Dexamethasone	Sigma Aldrich	D4902
Trizol reagent	Invitrogen / Life Technologies	15596026
DAPI	Vectashield; Vector Laboratories	H-1200
Lipopolysaccharides (LPS)	Sigma	L5418
X-tremeGENE transfection reagent transfection reagent	Roche	6366236001
TNF	Hiss	810167-B
TWEAK	PeproTech	310-06
zVAD-fmk	Millipore	627610
Nec-1	Biovision	2263
TPCA	Tocris	2559
PhosSTOP™	Roche	4906837001
cOmplete™ Protease Inhibitor	Roche	04693124001
Etanercept (Enbrel)	Pfizer	N/A
Software and Algorithms		
Tissue IA image analysis software	Leica	N/A
QuPath 0.3.0	University of Edinburgh	N/A
GraphPad Prism 8 Software	GraphPad	N/A
Bio-Plex Manager Instrument Control Version 6	Bio-Rad	N/A
DESeq2	Love et al.[64]	N/A
RQ manager 1.2	Applied Biosystems	N/A
SDS 2.3	Applied Biosystems	N/A
Imaris 8.1	Bitplane	N/A
Feature Extraction Software	Agilent	N/A
SPSS Statistics 25	IBM	N/A

RESOURCE AVAILABILITY

Lead contact

Further information and requests for resources and reagents should be directed to and will be fulfilled by the lead contact, Tom Luedde (luedde@hhu.de).

Materials availability

Mouse lines generated in this study are available upon signing a material transfer agreement.

Data and code availability

Single-cell RNA sequencing that support this study have been deposited in the GEO database: GSE166875. The aCGH data have been deposited into the ArrayExpress database: E-MTAB-4599 and the microarray data have been submitted to the Gene Expression Omnibus (accession number GSE80392).

EXPERIMENTAL MODEL AND SUBJECT DETAILS

Generation of conditional genetically ablated mice

Mice carrying LoxP-site-flanked alleles of *Traf2*[65] were crossed to *alfpAlb*-Cre transgenic mice[66] to generate LPC-specific ablated mice. Mice with combined conditional deletions of *Traf2* and *Casp-8*[67] or additional conditional deletion of *Mlkl*,[68] *Nemo*,[69] *Ikk*β,[70] *Ripk1*[71] or *Rela*,[72] or rather constitutive deletion of *Ripk3*[73] were generated by intercrossing the respective lines to LPC$^{\Delta Traf2,\ Casp8}$ mice. In all experiments, littermates carrying the respective loxP-flanked alleles but lacking expression of Cre recombinase were used as wild-type (WT) controls. Mice were bred on a mixed C57/BL6 - SV129Ola genetic background. Only sex- and age-matched animals were compared. All animal experiments were approved by the Federal Ministry for Nature, Environment and Consumers' Protection of the state of North Rhine-Westphalia and were performed in accordance to the respective national, federal and institutional regulations.

Human Liver Samples

The project was approved by the internal review board of the USZ and the Cantonal Ethics Committee of Zurich, Switzerland (approval no: PB_2018-002). Informed consent was obtained from all patients.

METHOD DETAILS

Liver Injury Models

Experiments were performed on 6-week-old female mice. LPS (Sigma-Aldrich) was administered intraperitoneally at 2.5 mg/kg of body weight.

Clodronate-Liposome Model

8-week-old male LPC$^{\Delta Traf2,\ Casp8}$ mice were injected intravenously with 200 μl of either clodronate-loaded or PBS-loaded liposomes (5 mg/ml) (Liposoma BV). The mice were sacrificed 48 hours after injection.

Anti TNF Treatment with Etanercept

12-14-week-old LPC$^{\Delta Traf2,\ Casp8}$ mice were treated with etanercept or vehicle (PBS) (s.c. injection was given every 3 days, 10 mg/kg) for a period of 2 weeks. The mice were sacrificed 24 hours after the last injection.

Primary Hepatocyte Culturing

Isolated primary hepatocytes from different mouse lines (6-12 week old) were cultured in Dulbecco's modified Eagle's medium (DMEM, PAN Biotech) supplemented with 10% fetal calf serum (FCS, PAN Biotech), penicillin (100 U/ml, PAN Biotech), streptomycin (0.1 mg/ml, PAN Biotech) and stimulated with recombinant TNF (50 ng/ml, HiSS) for the indicated time points.

The collagen coating as well as the thawing, counting and plating of primary human hepatocytes was done according to a published standard procedure.[74] Briefly, primary human hepatocytes were quickly thawed in a 37°C water bath and transferred into 5 ml/vial of warm plating medium in a 50 ml centrifuge tube. The cells were re-suspended by gently inverting the tube. The cell number and vitality was determined by preparing a tryptan blue staining and counting the cells in a Neubauer counting chamber. After adjustment for vitality 250,000 viable cells in 500 μl plating medium were plated per well of a collagen coated 4-well IBIDI chamber (80426, Ibidi, Gräfelfing, Germany) using a cut pipette tip. After 3-4h of attachment at 37°C and 5% CO_2, the cells were washed 3 times with 1x PBS and 0.5 ml of PHH culture medium was added per well. After overnight culture at 37°C and 5% CO_2 the medium was exchanged with PHH culture medium (Williams E medium supplemented with stable glutamine, 2.5 mM dexamethasone, ITS Supplement, Pen/Strep and gentamycin) containing 1 μg/ml TWEAK. After 25.5h of incubation at 37°C and 5% CO_2 20μM zVAD-fmk was added and the cells were incubated for further 45 minutes at 37°C and 5% CO_2, before the medium was exchanged with 0.5 ml/well staining solution 1 containing 1 μg/ml TWEAK and 20μM zVAD-fmk. Following a 15-minute incubation at 37°C and 5% CO_2, the medium was removed and the cells were washed one time with culture medium. Finally, 0.5 ml/well staining solution containing TWEAK (1 μg/ml), zVAD-fmk (20 μM) and TNFα (5 ng/ml) and the cells were imaged.

Magnetic-Activated Cell Sorting (MACS) using anti-CD45 Microbeads

Immunomagnetic cell separation was performed with the MACS system (Miltenyi Biotec) according to the manufacturer's protocol using anti-CD45 mouse MAb-conjugated microbeads (CD45 microbeads). In brief, isolated primary hepatocytes from 6-12 week old WT and LPC$^{\Delta Traf2,\ Casp8}$ mice were used and cells were resuspended in 90 μl MACS buffer (PBS pH 7.2, 0.5% BSA, and 2 mM EDTA) and incubated with 10 μL each of anti-mouse CD45 microbeads (Miltenyi Biotec; 130-052-301) at 4°C for 15 min (specific volume is per 10^7 cells). After a washing step, up to 10^8 cells were resuspended in 2ml MACS buffer and applied to LS columns (Miltenyi

Biotec; 130-042-401) in a QuadroMACS™ separator (Miltenyi Biotec). $CD45^+$ cells attached to the magnetized matrix in the column, and $CD45^-$ cells were washed out. The effluent cells were collected as the $CD45^-$ fraction, which contained enriched primary liver hepatocytes. The enriched primary hepatocytes were cultured overnight in William's Medium E containing 50 IU Penicillin-Streptomycin and 10% fetal bovine serum (FBS) and used for RNA extraction.

Traf2$^{-/-}$ MEF Culture

Traf2$^{-/-}$ MEFs were cultured in Dulbecco's modified Eagle's Medium (PAN Biotech) supplemented with 10% fetal bovine serum (FCS, PAN Biotech), penicillin (100 U/ml, PAN Biotech), streptomycin (0.1 mg/ml, PAN Biotech). Cells were pre-incubated with zVAD-fmk (20 μM) alone or in combination with necrostatin-1 (Nec-1, 10 μM) and or TPCA (20 μM) for 60 min and then stimulated with TNF (50 ng/ml, HiSS) overnight.

In Vitro Live Cell Imaging

Traf2$^{-/-}$MEFs were seeded in standard 12 well cell culture plates in 2ml [DMEM medium] and were subjected to *in vitro* time lapse microscopy, using an AxioObserver Z1 (Zeiss, Göttingen, Germany) modified with large chamber cell culture incubation unit (Pecon, Erbach, Germany). Cells were pre-incubated with Nec-1 (10 μM) alone or zVAD-fmk (20 μM) alone or zVAD-fmk was used in combination with Nec-1, (10 μM) or TPCA (20 μM) for 1 hour and then stimulated with TNF (50 ng/ml). Cells were followed over a time period of up to 24 hours, taking images from 8 different target positions within the well every 3 minutes. Cells were kept at 37°C and 5% CO_2 atmosphere over the time course of the experiment. Time lapse videos were generated using ZEN Blue 2.0 (Zeiss), statistical video image analysis and cell counting was performed using Imaris 7.7 (Bitplane, Zürich, Switzerland).

Serum-Analysis

Serum ALT, AST, GLDH, AP activities and total serum bilirubin were measured by standard procedures in the Laboratory Diagnostic Center (LDZ) of the RWTH University Hospital Aachen.

Western blot Analysis

Liver tissue was homogenized in NP-40 lysis buffer using a tissue grind pestle (Kontes) to gain protein lysates. These were resolved by reducing SDS-polyacrylamide gel electrophoresis (PAGE), transferred to PVDF membrane and analyzed by immunoblotting as previously described.[21] Membranes were probed with the respective primary antibodies listed in the key resources table. As secondary antibodies, rabbit-HRP, mouse-HRP (Amersham) were used.

Electrophoretic Mobility Shift Assay (EMSA)

Gel retardation assays were performed on nuclear extracts as described previously.[75] DNA protein complexes were resolved on a 6% polyacrylamide gel. A ^{32}P-labeled oligonucleotide representing an NF-κB consensus site (5'-CGG GCT GGG GAT TCC CCA TCT CGG TAC-3') was used as a probe. For supershifts, high-concentrated antibodies against p50 and p65 (Santa Cruz) were used.

Quantitative Real-Time PCR

Total RNA was purified from liver tissue using Trizol reagent (Invitrogen) and an RNeasy Mini Kit (Qiagen). The quantity and quality of the RNA was determined spectroscopically using a nanodrop (Thermo Scientific). Total RNA (1 μg) was used to synthesize cDNA using the Transcriptor cDNA First-Strand Synthesis Kit (Roche) according to the manufacturer's protocol, and was resuspended in 50 μl of H_2O. cDNA samples (2 μl) were used for real-time PCR in a total volume of 25 μl using SYBR Green Reagent (Invitrogen) and specific primers on a qPCR machine (Applied Biosystems 7300 Sequence Detection System). All real-time PCR reactions were performed in duplicates. Data were generated and analysed using SDS 2.3 and RQ manager 1.2 software. Primer sequences are available upon request. All values were normalized to the expression of beta-actin mRNA.

Stainings

Paraffin sections (2μm) were stained with H/E or various primary and secondary antibodies. Paraformaldehyde (4%) fixed and paraffin embedded liver tissue was incubated in Bond Primary antibody diluent (Leica) and staining was performed on a BOND-MAX immunohistochemistry robot (Leica Biosystems) using BOND polymer refine detection solution for DAB or BOND polymer refine red detection for AP, respectively. The following antibodies were used: Antibodies against F4/80 (BMA Biomedicals AG, 1:120), B220 (BD Pharmingen, 1:3000), CD3 (Zytomed, 1:250), CD206 (Serotec; 1:500), Cytokeratine19 (TROMAIIIc, Hybridoma bank, 1:250), SOX9 (Millipore, 1:250), RIPK3 (Enzo Life Sciences; 1:500), (pan-cytokeratin (Dako A/S; 1:300), Collagen IV (Cedarlane; 1:50), GP73 (Santa Cruz; 1:100), A6 (1:50) (antibody kindly provided by Dr. Valentina Factor, NIH, Bethedsda, Maryland, USA), Ki67 (NeoMarkers; 1:200), MIP3A/CCL20 (ABCAM; 1:20), Caspase-8 (Enzo; 1:200) and cleaved Caspase-3 (Cell Signaling; 1:300). Image acquisition was either performed on an Olympus BX53 microscope equipped with an Olympus DP72 digital camera or with a Leica SCN400 slide scanner.

TUNEL

The TUNEL staining on paraformaldehyde (4%) fixed and paraffin embedded liver tissue slides was performed according to the manufacturer's (Promega) protocol. Nuclei were visualized by using mounting medium containing DAPI (Vectashield; Vector Laboratories).

In situ hybridisation by RNAScope® Chromogenic

Five micrometer thick formalin-fixed paraffin-embedded (FFPE) sections from mouse livers or human liver biopsies were prepared for RIPK3 *in situ* hybridization using the RNAScope® 2.5 HD Detection Reagents-RED assay Kit (#322360; Advanced Cell Diagnostics). Mus musculus-RIPK3 or Human-RIPK3 probes (by Advanced Cell Diagnostics (ACD); ACD catalogue number #462541 and #434661 respectively) were used according to manufacturer's protocol to visualise RIPK3 RNA with Fast Red dye.

Transmission Electron Microscopy

Tissue was fixed in 3% glutaraldehyde (Agar scientific, Wetzlar, Germany) for at least 4h, washed in 0.1 M Soerensen's phosphate buffer (Merck, Darmstadt, Germany). Post-fixation of cells was performed in 1% OsO_4 in 17% sucrose buffer. After fixation, samples were washed in 17% sucrose buffer and deionized water and dehydrated by an ethanol series (30, 50, 70, 90 and 100%) for 10 min each and the last step thrice. The dehydrated specimens were incubated in propylene oxide (Serva, Heidelberg, Germany) for 30 min, in a mixture of Epon resin (Sigma) and propylene oxide (1:1) for 1h and finally in pure Epon for 1h. Samples were embedded in pure Epon. Epon polymerization was performed at 37°C for 12h and then 80°C for 48h. Ultrathin sections (70-100 nm) were cut with a diamond knife (Leica, Wetzlar, Germany) by an ultramicrotome (Reichert Ultradcut S, Leica) and picked up on Cu/Rh grids (HR23 Maxtaform, Plano, Wetzlar, Germany). Negative staining by uranyl acetate and lead citrate (all EMS, Munich, Germany) was performed to enhance TEM contrast. The specimens were viewed using a Zeiss Leo-906 electron microscope (Oberkochen, Germany), operated at an acceleration voltage of 60kV.

3D Reconstruction of the Biliary System

For 3D analysis, livers were fixed in 4% PFA for 2 hours at 4°C, washed in PBS, cryoprotected with increasing concentrations of 10%, 20%, and 30% sucrose solutions prepared in PBS, embedded in O.C.T. Tissue Tek, and sectioned. 75 μm thick cryosections were transferred to 24-well culture dishes and 1 ml PBS was added to allow the sections to thaw and to float in the buffer. After washing 4 x in PBS for 15 minutes, membranes were dissolved with permeabilization buffer (1% Triton-X/ PBS) for 2 hours at room temperature (RT). For blocking nonspecific antibody binding floating sections were incubated with blocking buffer (1% Triton-X/ PBS + 10% Serum) for 4 hours at 37°C. Sections were incubated with primary CK19 antibody for 48 hours at 4°C and washed 4 x 20 minutes (1%Triton-X/ PBS) before incubation with the secondary antibody for 48 hours at 4°C (anti-rat Alexa 488, 1:500). After washing (4 x 20 min 1% Triton-X/ PBS + 3 x 15 min PBS) diluted dye (ToPro3) for nuclear staining was incubated for 90 minutes at RT in PBS. Counterstained specimens were washed in PBS (3 x for 15 minutes) and covered in mounting medium. Confocal z-stacks (1 μm) were acquired on an Olympus FV10i microscope and 3D images were created/ analysed with Imaris 8.1 Software (Bitplane).

Array Comparative Genomic Hybridization (aCGH) Analysis

To characterize copy number alterations, oligo array CGH using the Agilent (Boeblingen, Germany) platform was performed. Genomic DNA was extracted from formalin-fixed paraffin-embedded (FFPE) tissue sections, after enrichment for tumor cells by micro-dissection, using the DNAeasy FFPE kit (Qiagen, Hildesheim, Germany). DNA extracted from 4 normal liver tissues was pooled and used as reference DNA. 250 ng of test and reference DNA were differentially labelled with Cy3-dUTP (test) and Cy5-dUTP (reference) by random primed labelling using the CGH labelling kit for oligo arrays (Enzo, Loerrach, Germany). Hybridization, washing and scanning was performed according to the manufacturer's protocol and the data were extracted from the Feature Extraction Software (Agilent, Boeblingen, Germany) as tab-delimited text files. The arrays used were custom-designed 8x60k arrays (AMADID 41078) with approx. 60000 probes covering the whole mouse genome. The probe set includes the Agilent 44k (AMADID 15028) in order to enable merging of the 60k data with 44k data. The raw data were imported into the R statistical platform (R Development Core Team. R: A language and environment for statistical computing. R Foundation for Statistical Computing, Vienna, Austria. ISBN 3-900051-07-0, URL: http://www.R-project.org/) and the background subtracted median intensity signals were used to build the $\log_2$ ratios. After median normalization values were quality filtered using flags as defined by the Agilent Feature extraction software. The $\log_2$ ratios were subsequently segmented, called and copy number regions were defined using functions from the CGHbase [Sjoerd Vosse and Mark van de Wiel (2011). CGHbase: Base functions and classes for arrayCGH data analysis. R package version 1.15.1.], CGHcall (Mark van de Wiel and Sjoerd Vosse (2012). CGHcall: Calling aberrations for array CGH tumor profiles. R package version 2.17.5) and CGHregions (Sjoerd Vosse & Mark van de Wiel (2009). CGHregions: Dimension Reduction for Array CGH Data with Minimal Information Loss. R package version 1.14.0. Bioconductor packages). For the CGHcall function 75% estimated proportion of tumor cells based on microscopic assessment of Haematoxylin stained FFPE sections, was used. The copy number profiles were karyogram plotted using an in-house written R function. The aCGH data have been deposited into the ArrayExpress database under accession number E-MTAB-4599 (http://www.ebi.ac.uk/arrayexpress/). The genomic positions of the copy number regions which were mm9 were transformed to mm10 genome assembly using UCSC LiftOver and assigned to genes using the R package biomaRt. Cancer-related genes were identified using the COSMIC Cancer Gene Census database (version June 2020).

Micro-Array

RNA was purified from mouse livers using TRIzol (Life Technologies, Calsbad, CA, USA) followed by an additional round of purification with RNeasy Microkit columns (Qiagen, Venlo, the Netherlands). RNA quality was assessed using RNA 6000 nanochips on the Agilent 2100 bioanalyzer (Agilent Technologies, Amsterdam, the Netherlands). Purified RNA (100 ng) was labeled with the Affymetrix WT PLUS reagent kit (Affymetrix, Santa Clara, CA, USA) and hybridized to an Affymetrix Mouse Gene 1.1 ST array plate (Affymetrix). Hybridization,

washing and scanning were carried out on an Affymetrix GeneTitan platform according to the manufacturer's instructions. Microarray analysis was performed using MADMAX pipeline for statistical analysis of microarray data.[76] Arrays were normalized using the robust multiarray average method.[77,78] Probe sets were defined according to Dai et al.[79] In this method probes are assigned to Entrez IDs as a gene identifier. The P values were calculated using an intensity-based moderated t-statistic (IBMT); $p < 0.01$ was considered significant.[80] The microarray data have been submitted to the Gene Expression Omnibus (accession number GSE80392).

RNA Sequencing

We performed RNA-seq (poly-A prepped libraries) on 15 fresh frozen samples (11 tumor tissue derived from 52-55 week aged $LPC^{\Delta Traf2,\ Casp8}$ mice, and 4 liver samples from wild-type mice). Starting material was 1 μg of total RNA extracted using RNeasy Mini Kit (Qiagen). RNA integrity was checked by the 2100 Bioanalyzer using the RNA 6000 Nano assay (Agilent, CA, USA). All processed total RNA samples had RIN value of 7.0 or greater. The sequencing library was prepared with the standard TruSeq RNA Sample Prep Kit v2 protocol (Illumina, CA, USA). Briefly, mRNA was isolated and fragmented. cDNA was synthesized using random hexamers, end-repaired and ligated with appropriate adaptors for sequencing. The library then underwent size selection and purification using AMPure XP beads (Beckman Coulter, CA, USA). The appropriate Illumina recommended 6 bp barcode bases were introduced at one end of the adaptors during PCR amplification step. The size and concentration of the RNAseq libraries was measured by Bioanalyzer and Qubit fluorometry (Life Technologies, NY, USA) before loading onto the sequencer. The mRNA libraries were sequenced on the Illumina HiSeq 2500 System with 100 nucleotide single-end reads, according to the standard manufacturer's protocol (Illumina, CA, USA). Sequencing was performed using an Illumina HiSeq Sequencer.

RNA-seq data were normalized and tested for differential expression as implemented in the R package DESeq2.[64,81] We used independent filtering to reduce the penalty for multiple testing and out of 19,451 genes with non-zero counts, we filtered outliers as identified using Cook's distance (456 genes, 2.3%) and those with generally low counts (mean count <1.3; 2,823; 15%). We used hierarchical clustering and PCA for exploratory data analysis. To gain functional insight on the affected pathways and biological processes, we did Gene Set Enrichment Analysis[82] of pre-ranked gene lists weighted by the log-fold change from the previous differential expression tests. Interrogated gene sets (n=123) included Hallmark, Liver Cancer Signatures, NF-κB-related and Hedgehog-related as available at the Molecular Signature Database (http://software.broadinstitute.org/gsea/msigdb) from the Broad Institute. Raw data for the RNA-seq experiments are deposited on ArrayExpress (www.ebi.ac.uk/arrayexpress) under accession number E-MTAB-4598. The Necroptosis Gene Signature was generated using human orthologues of differentially expressed genes (FDR < 0.05, Fold-change > $\log_2$ 2) between

$LPC^{\Delta Traf2,\ Casp8}$ tumors and non-tumoral tissue from $LPC^{\Delta Traf2,\ Casp8}$, $Ripk3^{-/-}$ liver. The signature was evaluated in a cohort of 228 human HCC samples treated with surgical resection for which whole-genome microarray data (Affymetrix U219) was available.[42] Signature predictions were done using the Nearest Template Prediction method.[83] Raw data for the human microarrays are deposited on GEO Omnibus accession number GSE63898. Kaplan-Meier curves (log-rank test) were used for the clinical correlation with patient's outcome.

Single Cell RNA Processing, Clustering and Annotation

Immune cells were freshly isolated from the liver of 3 mice per group and sorted as $CD45^{+}CD31^{-}$ by fluorescence activated cell sorting (FACS) using Aria-II (BD Biosciences). Isolated cells from each group were pooled and washed once with cold phosphate-buffered saline (PBS) + 0.1% bovine serum albumin (BSA) and subjected to single-cell RNA sequencing analysis using the Chromium System (10x Genomics, California, USA). Per sample, 7000 cells were used with a recovery rate of about 60%. Sequencing was performed on Illumina NextSeq 550 (paired-ends, 2×75 bp), resulting in 60 000 reads per cell and $\sim 4 \times 10^8$ total reads per Illumina chip. Primary data analysis was performed with 10x Genomics Cell Ranger (version 3.0.1). Sequenced reads were aligned to the mouse genome reference sequence GRCm38 (version 93) as standardly preprocessed by 10x (preprocessed version 3.0.0). The downstream analysis was performed using Seurat (Version 2.3.4).[84] A Seurat object first was created from the raw read counts. Next, we filtered the data to remove the impact of low quality cells and doublets. We retained only cells with the total expressed genes in between 100 and 3000 and cells with mitochondria or ribosome content is less than 50%. The data was then log-normalized and scaled to regress out the effects of nUMI and percentage of mitochondrial and ribosome content. Next, we selected the top 1000 variable genes for further analysis. Dimension reduction method Principal Component Analysis (PCA) was performed to reduce the dimension. Next, we performed SNN based clustering with parameter resolution=0.45 on the top 30 PCs, followed by t-distributed stochastic neighbor embedding (t-SNE) to visualize clusters. Then clusters were manually annotated based on marker genes found by FindAllMarkers functions. To inspect presence of monocytes and monocyte-derived macrophages, we subset the data to keep only MoMF and KC clusters and re-run t-SNE with a perplexity of 90. Next, we looked for markers (FindMarkers) by comparing KC vs. MoMF I, MoMF II and MoMF I, MoMF II vs. MoMF III. Next, we performed a heatmap with ComplexHeatmap[85] (with default parameters) only considering genes highly expressed in MoMF I, MoMF II (average log-FoldChange>=1.5).

Measurement of Cytokines

Cytokines from mouse serum or cell culture supernatants were measured using suspension bead array immunoassay kits following the manufacturer's specifications. TNF, IL-6 and MCP-1 were measured with the Bio-Plex Pro Mouse Cytokine GrpI panel, (Bio-Rad) or MCYTOMAG-70K (Millipore) on a Luminex® 100/200 analyser. The data were analyzed with Bio-Plex Manager Instrument Control Version 6 (Bio-Rad).

Determination of CCL20 Concentrations by ELISA

CCL20 (R&D/MCC200) serum concentrations were analyzed using commercial enzyme immunoassays according to the manufacturer's instructions.

Intravital Imaging

Intravital imaging of mouse livers was done using an inverted two-photon microscope (LSM MP7- Zeiss, Jena, Germany) with an LD C-Apochromat 40 × 1.1 water immersion objective, according to the method originally described by Reif et al.[86] with modifications.[49] Briefly, mice were anesthetized by intraperitoneal injection of ketamine (100 mg/kg b.w.), xylazine (10 mg/kg b.w.), acepromazine (1.7 mg/kg b.w.) and buprenorphine (0.08 mg/kg b.w.). In order to record cell death/leakiness, the following functional dyes were intravenously-administered: Hoechst 33258 (further referred to as 'Hoechst', 5 mg/kg), rhodamine 123 (further referred to as rhodamine, 0.8 mg/kg), tetramethylrhodamine ethyl ester (TMRE, 0.96 mg/kg), propidium iodide (PI, 2.67 mg/kg, MW: 668 Da), SYTOX green (1.2 mg/kg, MW: 600 Da), and Texas red-coupled dextran 3000 (2 mg/kg, MW: 3000 Da); all from Thermo Fisher Scientific, Germany. In addition, a catheter (SAI Infusion Technologies, USA) was placed into the tail vein of mice for administration of cholyl-lysyl-fluorescein (CLF; Corning, USA, 1 mg/kg) during the recording. Subsequently, the left liver lobe was exposed by a midline incision in the abdominal wall caudal to the sternum, and placed onto a 0.17 mm-thick cover slip (Logitech, UK) in a custom-made platform, and then fitted into the microscope stage. In order to avoid dehydration during long-term recordings, the exposed liver lobe was covered with a saline-moistened gauze. Finally, a maintenance isoflurane inhalation anaesthesia (1-2%) was applied during the entire recording period.

Image Analysis and Statistical Evaluation

Calculation of mean fluorescence intensity in the sinusoids, the cytoplasm and the nuclei of hepatocytes was determined in specified regions of interest (ROIs), as indicated in the result section, using ZEN software (Zeiss, Jena, Germany). All videos and analyzed ROIs are available in the supplements. For analysis of PI-/SYTOX Green-associated fluorescence the nuclear area was defined based on the Hoechst signal. Recording of fluorescence was performed between 30 and 40 min after i.v. injection of PI or SYTOX Green. For each mouse model at least 600 nuclei from 3-9 mice were analyzed for each analysis type. Texas Red-coupled dextran (3000 MW) was i.v. injected and the associated fluorescence was recorded within 12 minutes afterwards. Hepatocytes were identified based on the rhodamine signal to quantify the intensity of dextran-associated fluorescence. For analysis of the time until loss of mitochondrial potential, mice received i.v. injections of PI/SYTOX green, rhodamine/TMRE and Hoechst and relatively long imaging periods of ~400 minutes were recorded. All hepatocytes with PI/SYTOX Green positive nuclei were identified based on their rhodamine/TMRE signal. Only PI/SYTOX Green positive, rhodamine/TMRE positive hepatocytes were included into the follow-up analysis. Events of mitochondrial potential loss were defined by loss of all visible rhodamine/TMRE-associated fluorescence. The time until mitochondrial potential loss was analysed by Kaplan-Meier statistics. Kaplan Meier analyses, frequency plots and Spearman correlation coefficients were calculated by SPSS Statistics 25.

QUANTIFICATION AND STATISTICAL ANALYSIS

Statistics

Data were analyzed using PRISM software (GraphPad Prism 8 Software, Inc., La Jolla, CA) and are expressed as mean. Statistical significance between experimental groups was assessed using unpaired two-sample t-test, Mann-Whitney test, ANOVA or Kruskal Wallis respectively.

Analysis and Quantification of Immunohistochemical Stainings and TUNEL

For quantification of stainings, whole slides were scanned using a SCN400 slide scanner (Leica) and analyzed using Tissue IA image analysis software (Leica) with optimized quantification algorithms and normalized to the total cell number. Hepatocytes, bile ducts and oval cells were quantified for CCL20 expression in five high power fields (magnification 200x; 0= negative, 1= weak, 2=moderate, 3=strong). Overall positivity was calculated as the average score of the different epithelial cells combined.

RIPK3 IHC was analysed using QuPath 0.3.0.[87] Briefly, 4-6 liver regions ($\geq$0.78 mm^^{2}) were manually annotated and hepatocytes detected by watershed cell-segmentation at 20x with a nuclear area $\geq$35 μm^^{2}. Detections were expanded 5 μm delimited by shape, thereafter RIPK3-associated DAB optical density was measured. An average of 1658 hepatocytes were analysed from each mouse. Caspase-8 IHC (hepatocytes) was analysed using QuPath 0.3.0 (Bankhead et al.[87] [https://doi.org/10.1038/s41598-017-17204-5]). Briefly, 4-6 liver regions ($\geq$0.78 mm^2) were manually annotated and hepatocytes detected by watershed cell-segmentation at 20x with a nuclear area $\geq$35 μm^2. Detections were expanded 5 μm delimited by shape, thereafter Caspase-8-associated DAB optical density was measured. Caspase-8 (NPCs, positive area %) was analysed with Fiji/ImageJ 1.52e (Schindellin et al.[88] [https://doi.org/10.1038/nmeth.2019]) from colour deconvoluted DAB stain. Briefly, liver regions used for previous analysis were used for automatic segmentation by "Yen" threshold. Signal areas larger than 5 pixels were included in the analysis. TUNEL positive cells were counted manually from 6 view fields per animal (magnification 20x).